International Journal of Concrete Structures and Materials

RESEARCH

Open Access

Enhancing the Buildability of CSA Cement/OPC-Blended Mortar in 3D Printing: Optimizing CSA Cement and Water Contents Using a Statistical Approach

Sangwoo Oh[1], Jinsuk Lee[2] and Seongcheol Choi[1*]

Abstract

This study examined the influence of the water–binder ratio and calcium sulfoaluminate (CSA) cement replacement on the properties of fresh three-dimensional concrete printing (3DCP) materials and identified optimized mix proportions to enhance buildability. Experimental analyses included flowability tests, setting time evaluations, green strength assessments, extrusion pressure measurements, and printing tests. Buildability was evaluated using layer strain and interlayer bonding performance as key indicators, while statistical techniques were applied to develop a mixture design that maximized buildability and minimized the number of printing tests required. The experimental results showed that layer strain increased with a higher water–binder ratio and a lower CSA cement replacement ratio, and a similar trend was observed for interlayer bonding performance. The optimized mixture was determined using response surface methodology based on 13 experimental runs, yielding a water–binder ratio of 0.297 and a CSA cement replacement ratio of 3.88%. Verification results indicated that the optimized mixture exhibited superior buildability, with a mean relative error of 7.55% between the measured and predicted values, demonstrating close agreement between actual performance and predicted outcomes. These findings confirmed that the optimization process was effective and practically sound for enhancing the buildability of 3DCP materials.

Keywords 3D concrete printing (3DCP), Buildability, Calcium sulfoaluminate (CSA), Statistical approach, Water–binder ratio

1 Introduction

Three-dimensional concrete printing (3DCP) is an advanced manufacturing process in which structures are fabricated layer by layer using cement-based materials guided by three-dimensional model data (Buswell et al., 2018; Paul et al., 2018). This technique offers distinct advantages over conventional construction methods, including the ability to produce complex geometries and reduce construction time and cost (De Schutter et al., 2018; Paul et al., 2018). Consequently, 3DCP has attracted significant attention in the construction industry, with the number of related studies steadily increasing each year (Strohle et al., 2023). Research in this field encompasses design, materials, and construction processes, among which material development remains particularly challenging. From a material standpoint, 3DCP mixtures must exhibit smooth extrusion (extrudability) while maintaining structural integrity under the

Journal information: ISSN 1976-0485/eISSN 2234-1315

*Correspondence:
Seongcheol Choi
schoi@cau.ac.kr
[1] Department of Civil and Environmental Engineering, Chung-Ang University, 84 Heukseok-Ro, Dongjak-Gu, Seoul 06974, Republic of Korea
[2] Department of Smart Cities, Chung-Ang University, 84 Heukseok-Ro, Dongjak-Gu, Seoul 06974, Republic of Korea

© The Author(s) 2026. **Open Access** This article is licensed under a Creative Commons Attribution-NonCommercial-NoDerivatives 4.0 International License, which permits any non-commercial use, sharing, distribution and reproduction in any medium or format, as long as you give appropriate credit to the original author(s) and the source, provide a link to the Creative Commons licence, and indicate if you modified the licensed material. You do not have permission under this licence to share adapted material derived from this article or parts of it. The images or other third party material in this article are included in the article's Creative Commons licence, unless indicated otherwise in a credit line to the material. If material is not included in the article's Creative Commons licence and your intended use is not permitted by statutory regulation or exceeds the permitted use, you will need to obtain permission directly from the copyright holder. To view a copy of this licence, visit http://creativecommons.org/licenses/by-nc-nd/4.0/.

self-weight of successive layers and gravitational forces (buildability) (Oh et al., 2021; Zhang et al., 2021).

To overcome these challenges, researchers have investigated the incorporation of additives such as nano-attapulgite clay, rice husk ash, and calcium sulfoaluminate (CSA) cement to improve buildability without compromising extrudability (Marchon et al., 2018; Muthukrishnan et al., 2021; Reiter et al., 2020). Among these additives, CSA cement is particularly notable for its ability to enhance setting control even when used in small replacement ratios, thereby minimizing the need for extensive modifications to the overall mixture composition (Bhattacherjee et al., 2021). This improvement arises from the main phase of the CSA cement, ye'elimite ($C_4A_3\overline{S}$), which hydrates to produce monosulfoaluminate ($C_3A \cdot 3C\overline{S} \cdot 12H$), gibbsite ($AH_3$), and ettringite ($C_3A \cdot 3C\overline{S} \cdot 32H$). These hydration reactions promote early hardening (Huang et al., 2019; Park et al., 2021; Pelletier-Chaignat et al., 2011; Zhang et al., 2018). In addition, the volumetric expansion associated with ettringite formation mitigate shrinkage in 3D-printed materials—an issue arising from exposure to external air and high binder content—thereby improving structural stability (Huang et al., 2019; Park et al., 2021; Zhang et al., 2018).

Recent studies have further explored the role of CSA cement in facilitating rapid setting in 3DCP materials through partial binder replacement. Khalil et al. (Khalil et al., 2017) analyzed the effects of CSA cement replacement on heat of hydration, setting time, and compressive strength. Their manual stacking test using a silicon gun demonstrated that a mixture of 100% ordinary Portland cement (OPC) could form only five layers, whereas substituting 7% OPC with CSA cement enabled stacking up to 30 layers. Mohan et al. (Mohan et al., 2021) examined the initial hydration, rheological properties, and pumping characteristics of CSA cement mortars compared to OPC mortars. Their printing experiments with a 100% OPC mixture, an 80% CSA cement–20% limestone mixture, and a 70% CSA cement–30% limestone mixture revealed that the critical heights of the latter two were 7.0% and 3.6% higher than that of the pure OPC mixture. Similarly, Jiang et al. (Jiang et al., 2022) replaced 3%, 5%, 7%, and 10% of OPC with CSA cement and conducted slump flow, shape stability, penetration resistance, rheology, extrusion, and heat of hydration tests. Their findings indicated that increasing the CSA cement content decreased the mixture fluidity but enhanced buildability due to the stiffening effect.

Previous studies have primarily examined the application of CSA-incorporated cement-based materials for 3DCP using experimental approaches, such as rheological and printability tests. However, excessive replacement of OPC with CSA cement often results in poor layer quality or extrusion failure, indicating that stable printing performance can only be achieved with a narrow dosage range. Although an optimal replacement level is likely to exist, research directly addressing this issue remains limited. Furthermore, printing experiments are inherently time-consuming and labor-intensive, making trial-and-error methods inefficient for practical optimization. Recent advancements in the systematic optimization of 3DCP material design (Li et al., 2022; Liu et al., 2019; Sergis & Ouellet-Plamondon, 2022) suggest that a structured and quantitative methodology could more effectively identify suitable CSA cement replacement ranges and maximize their potential benefits. Nevertheless, previous research has not comprehensively analyzed how small variations in CSA cement content influence critical printability parameters, such as pumpability, extrudability, and buildability. Even minor adjustments in CSA cement dosage can either enhance extrusion stability or induce interlayer discontinuity and deformation failure. Therefore, further investigation is required to quantitatively evaluate these sensitive effects of CSA cement incorporation and to establish an efficient framework for determining replacement levels that achieve desirable printability and structural performance.

Buildability is a critical parameter in 3DCP materials (Oh et al., 2021; Paul et al., 2018; Strohle et al., 2023; Zhang et al., 2021), because it determines the feasibility of accurately transforming digital models into physical structures. Although the incorporation of CSA cement has been shown to enhance buildability (Jiang et al., 2022; Khalil et al., 2017; Mohan et al., 2021), such improvement is only meaningful when the printed structure exhibits both deformation-free stacking and satisfactory post-printing quality, including adequate interlayer bonding performance. For instance, materials with high thixotropic behavior may achieve good stacking stability during printing but may experience reduced structural performance if interlayer bonding is insufficient, potentially leading to defects, such as cold joints (Roussel, 2018). Therefore, when CSA cement is used as a partial binder replacement to enhance buildability, it is crucial to select an appropriate replacement ratio that avoids excessive stiffening and carefully evaluate its potential adverse effects on interlayer bonding. This study aims to identify an optimized mixture that maximizes buildability through partial binder replacement with CSA cement. The buildability evaluation considers both structural stability against layer deformation and post-printing quality, particularly interlayer bonding performance. To achieve this objective, statistical optimization methods are applied to determine a practically feasible and systematically refined mixture

Table 1 Chemical compositions of the cements used in this study (mass%)

	OPC	CSA cement
CaO	61.8	41.7
SiO_2	21.2	6.1
Al_2O_3	5.4	32.0
Fe_2O_3	3.2	2.4
MgO	2.4	2.6
SO_3	2.1	7.2
K_2O	0.7	0
Na_2O	0.1	0
TiO_2	0	1.6
Total	99.8	99.4

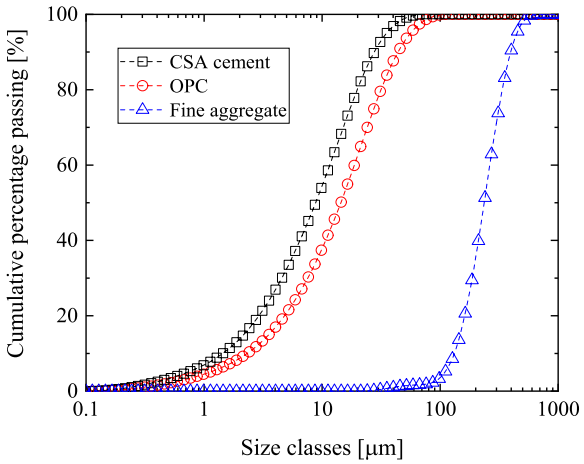


Fig. 1 Particle size distributions of CSA cement, OPC, and fine aggregates

design while minimizing the need for extensive printing experiments.

2 Experiment

2.1 Materials

The OPC used in this study had a fineness of 3,499 cm^2/g and a density of 3.13 g/cm^3, whereas the CSA cement exhibited a higher fineness of 5,750 cm^2/g and a lower density of 2.90 g/cm^3. Table 1 summarizes the chemical compositions of the OPC and CSA cements. Fine-grained feldspar with a density of 2.6 g/cm^3 was selected as the fine aggregate. Feldspar is inexpensive and readily available in South Korea. Its fine particle size facilitates continuous material flow while minimizing the risk of clogging during extrusion, making it functionally and industrially suitable for 3DCP applications (Kim et al., 2025). The particle size distributions of the CSA cement, OPC, and fine aggregates were analyzed using a laser diffraction particle analyzer (Mastersizer 3000, Malvern Panalytical Ltd., Malvern, UK). The measured d_{50} values were 10.0 μm for CSA cement, 16.3 μm for OPC, and 268 μm for the fine aggregate (Fig. 1). The superplasticizer (SP) used in the mixture was a polycarboxylate ether-based product (EcoCrete, ECONEX® Co., Ltd., Seoul, Republic of Korea) with a density of 1.06 g/cm^3 and a pH of 6.5. A methyl hydroxyethyl cellulose-based viscosity-modifying agent (VMA) (Combizell® LH20M, Tianpu Chemicals Co., Ltd., Zhangjiagang, Jiangsu Province, China) with a viscosity of 20,000 mPa·s and a density of 0.35 g/cm^3 was also used. The SP improved the flowability and pumpability of the mixtures, whereas the VMA increased the viscosity to prevent segregation and maintain shape stability after extrusion.

2.2 Mix Design

The mixture proportions of the specimens are presented in Table 2. In the specimen identification codes, "C" denotes "CSA cement" and the number following it indicates the binder replacement percentage. The number after the hyphen represents the water–binder ratio. To ensure adequate pumpability and extrudability, the dosages of SP and VMA were fixed at 1.65% and 0.2% of the total binder weight, respectively. The water–binder ratio and CSA cement replacement ratio were selected as the primary variable parameters. To maintain sufficient open time for the 3D printer used in this study, the CSA cement replacement ratio was restricted to below 5%. Preliminary trials indicated that mixtures containing more than 5% CSA cement exhibited excessively short open times under the given printing configuration, SP and VMA dosages, and aggregate-to-binder ratio, resulting in premature stiffening and printing interruptions. Accordingly, the CSA cement replacement levels were set at 0%, 2%, and 4%, while the water–binder ratios were fixed at 0.28, 0.30, and 0.32. The dosage levels of SP and VMA, as well as the parameter ranges for CSA cement and water–binder ratios, were determined based on preliminary experimental evaluations. As the primary objective of this study was to achieve the desired buildability through fine-tuning of printable mixture compositions, the selected specimens were first verified in preliminary trials to ensure both extrudability and buildability for the targeted printed elements. All specimens were prepared following the standard mixing procedures specified in ASTM C305 (ASTM, 2020).

2.3 Test Method

To comparatively evaluate the performance of each specimen, the experimental program was categorized into two groups: material tests without printing (Sects. 2.3.1–2.3.3) and printing-based tests (Sects. 2.3.4 and 2.3.5). For 3DCP materials, the mixture must exhibit sufficient pumpability and extrudability in the fresh

Table 2 Mixture proportions of the specimens

Specimen ID	OPC [kg/m^3]	CSA cement [kg/m^3]	Fine aggregate [kg/m^3]	Water [kg/m^3]	SP [kg/m^3]	VMA [kg/m^3]
C0-0.28	696.6	–	851.4	195.0	11.5	1.4
C2-0.28	682.4	13.9	851.1	195.0	11.5	1.4
C4-0.28	668.2	27.8	850.8	194.9	11.5	1.4
C0-0.30	687.0	–	839.7	206.1	11.3	1.4
C2-0.30	673.0	13.7	839.4	206.0	11.3	1.4
C4-0.30	659.1	27.5	839.1	206.0	11.3	1.4
C0-0.32	677.7	–	828.3	216.9	11.2	1.4
C2-0.32	663.9	13.5	828.0	216.8	11.2	1.4
C4-0.32	650.1	27.1	827.7	216.7	11.2	1.4

state to enable continuous and uniform extrusion while maintaining adequate buildability to prevent collapse or excessive deformation until the intended element is completed (Zhang et al., 2021). Accordingly, the material tests included a flow table test and setting time measurement (Sect. 2.3.1) to evaluate flowability and early age hydration behavior. In addition, a green strength test (Sect. 2.3.2) was conducted to compare the load-bearing capacity of the fresh mixtures, and an extrusion pressure test (Sect. 2.3.3) was performed to assess the pressure required during pumping. The extrusion pressure test was based on the slug test concept, which has been introduced for the inline evaluation of yield stress at the nozzle exit (Ducoulombier et al., 2021; Kolawole et al., 2022). While previous studies have used slug mass to estimate yield stress, the measured extrusion pressure was used as a comparative indicator of pumpability among mixtures in this study, a trend that has also been validated in other 3DCP research (Yin et al., 2023). Sections 2.3.4 and 2.3.5 present the evaluations based on printing. Although no standardized test method currently exists for assessing buildability, previous studies typically measured either the maximum printable height or the degree of layer deformation (Jiang et al., 2022; Tran et al., 2024, 2025). In this study, all mixtures were confirmed to be printable for the target element through preliminary trials, but notable differences were observed in layer deformation and interlayer bonding characteristics. Therefore, layer strain and interlayer bonding performance were selected as key indicators of buildability. To evaluate layer strain, printed specimens were cut perpendicular to the printing direction, and the cross-sectional layer widths were measured to quantify deformation. For interlayer bonding performance, the test configuration referenced RILEM TC 304-ADC guidelines (Wolfs et al., 2025) to ensure consistency with ongoing standardization efforts and to support comparability with future studies. Interlayer bonding performance was influenced by several interacting factors, including surface moisture condition, interface roughness, thixotropic structural build-up, and the time interval between successive layer depositions.

2.3.1 Material Experiment: Fluidity and Setting Time Tests

Fluidity is a critical factor affecting the printability of 3DCP materials; however, their relatively high stiffness makes traditional slump testing inappropriate when relying solely on gravitational force. Therefore, the fluidity of each specimen was evaluated immediately after mixing according to ASTM C1437 (ASTM 2020). To ensure the reliability of the measurements, at least three samples were tested for each mixture. Given that the incorporation of CSA cement accelerates the setting process, penetration resistance tests were conducted to examine its influence on setting characteristics. These tests were performed immediately after mixing according to ASTM C403 (ASTM 2023). All specimens were stored in a controlled environment maintained at a temperature of 20 ± 3℃ and a relative humidity (RH) of 50 ± 5%. For consistency and accuracy, a minimum of three samples were tested for each specimen.

2.3.2 Material Experiment: Green Strength Test

The green strength test was conducted to evaluate the mechanical behavior of each specimen in the fresh state in accordance with ASTM D2166 (ASTM, 2024). The procedures from specimen preparation to testing are shown in Fig. 2. To facilitate specimen removal, an acrylic cylindrical mold with an inner diameter of 70 mm and a height of 140 mm was lined with a Teflon sheet. The mold was placed on a plate covered with a Teflon sheet and filled with the test material. To ensure homogeneity, the material was compacted using vibratory consolidation. The test was performed using a universal testing machine (UTM) at a loading rate of 30 mm/min in the compaction direction until a strain level of 25% was reached. Measurements were taken at 30, 60, 90, 120, 150, and 180 min

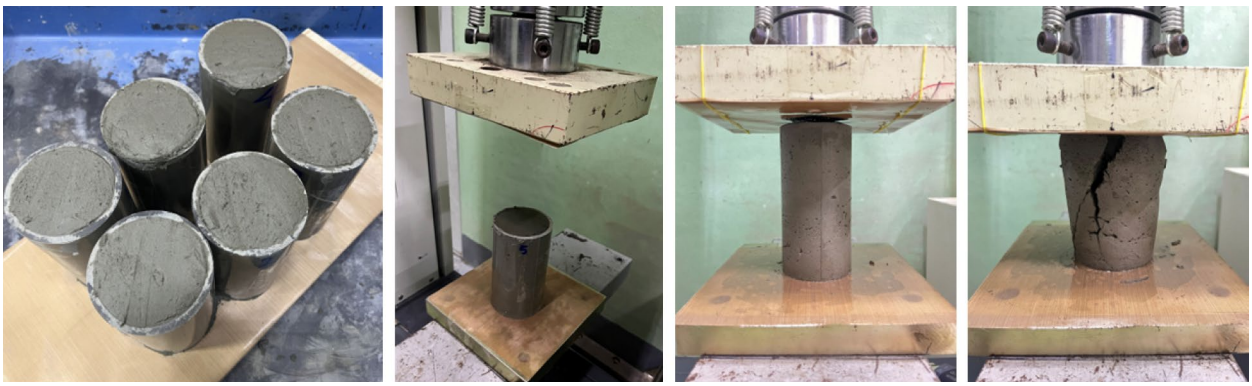


Fig. 2 Procedure for the green strength test for each specimen: (**a**) consolidation of the material using a vibration device immediately after mixing, (**b**) placement of the sample in the UTM, (**c**) initiation of loading, and (**d**) failure of the sample after testing



Fig. 3 Schematic of the extrusion pressure test setup

after the initial water–binder contact. To prevent premature deformation, each specimen was transferred to the UTM platen while still contained within the mold. The mold was then gently removed immediately before testing, and a Teflon sheet was placed on the platen to ensure a free-support condition.

2.3.3 Material Experiment: Extrusion Pressure Test

The custom-designed setup for measuring extrusion pressure is shown in Fig. 3. To compare the extrusion pressures required for different mixtures, a cylinder with a circular outlet of 20 mm in diameter was filled with freshly mixed material and compacted to ensure uniform consistency. Extrusion was performed using a UTM, which applied displacement to a cylindrical piston with a diameter of 104.5 mm at a constant rate of 1 mm/s. The maximum force recorded during the extrusion of each slug was designated as the extrusion pressure. For each specimen, a minimum of ten slugs were tested, and the average extrusion pressure was calculated to enable comparison among mixtures. The tests were conducted at 15, 35, and 65 min after the initial water–binder contact.

2.3.4 Printing Experiment: Layer Deformation

The printing equipment used in this study is shown in Fig. 4. The system is a gantry-type concrete 3D printer capable of constructing elements with dimensions of 1 m × 1 m × 1 m. To facilitate observation of layer deformation, a circular nozzle outlet with a diameter of 17 mm was used. The nozzle travel speed was set to 1000 mm/min, and all specimens were printed as ten-layer structures with a length of 300 mm. After printing, the specimens were cured under controlled conditions of 20 ± 3℃ and 50 ± 5% RH for 24 h. After curing, each specimen was vertically sectioned using a concrete saw to expose the cross section. Layer strain was calculated by comparing the average widths of the 7th, 8th, and 9th layers with those of the 2nd, 3rd, and 4th layers, as expressed in Eq. (1). Figure 5 presents representative printed specimens and their corresponding cross sections. The 10th layer was excluded from the analysis due to potential inaccuracies that arise during the final stages of printing, when material discharge and nozzle motion become less stable. Similarly, the first layer was excluded, because its deformation behavior differed from that of the remaining layers as a result of friction with the printing bed and variations in the nozzle stand-off distance:

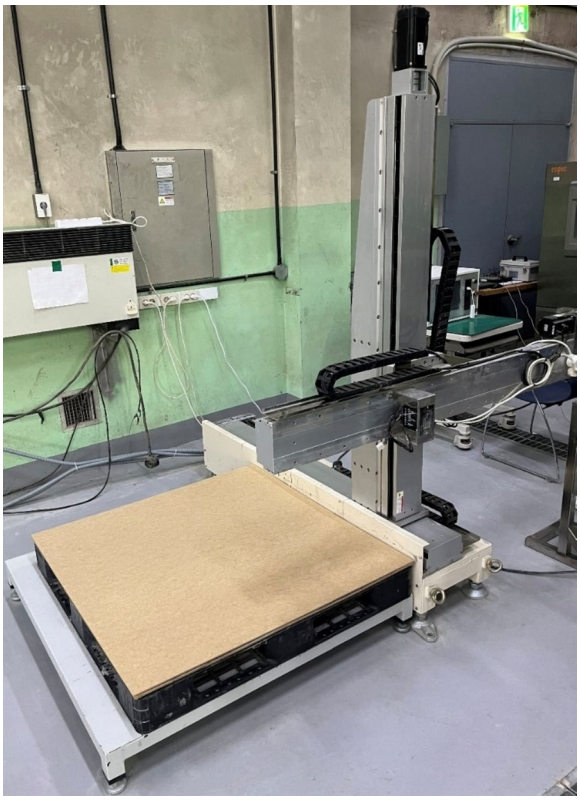


Fig. 4. 3D concrete printer with a build area of 1 m×1 m×1 m (W×L×T)

$$\varepsilon_{layer} = \frac{(w_2 + w_3 + w_4) - (w_7 + w_8 + w_9)}{(w_7 + w_8 + w_9)} \quad (1)$$

where ε_{layer} is the layer width strain [-], and w_2, w_3, w_4, w_7, w_8, and w_9 represent the average widths [mm] of the 2nd, 3rd, 4th, 7th, 8th, and 9th printed layers, respectively.

2.3.5 Printing Experiment: Interlayer Bonding Performance

A circular nozzle with an outlet diameter of 21 mm was used for the printing experiment and mounted on the 3D printer shown in Fig. 4. The specimens were printed with a layer width of 40 mm and a length of 600 mm. After curing for 24 h, the printed samples were cut into prisms measuring 40×40×160 mm using a concrete saw. For comparison, the same material was also cast into 40×40×160 mm molds and cured under the same conditions as the printed samples. Following the initial curing period, all prisms were air-cured at 20 ± 3℃ and 50 ± 5% RH for 24 h, and then submerged in water at 20 ± 3℃ from the age of 1 day until testing. Flexural strength tests were performed in accordance with ASTM C78 (ASTM 2022) at 3, 14, and 28 days. The interlayer bonding performance (*IBP*) of the printed specimens was calculated using Eq. (2), which relates the flexural strengths of the printed prisms to that of the cast prisms. Figure 6 shows the saw-cutting procedure used to prepare the printed prisms, as well as representative fractured printed prisms after testing:

$$IBP = \frac{f_{r,printed}}{f_{r,cast}} \times 100(\%) \quad (2)$$

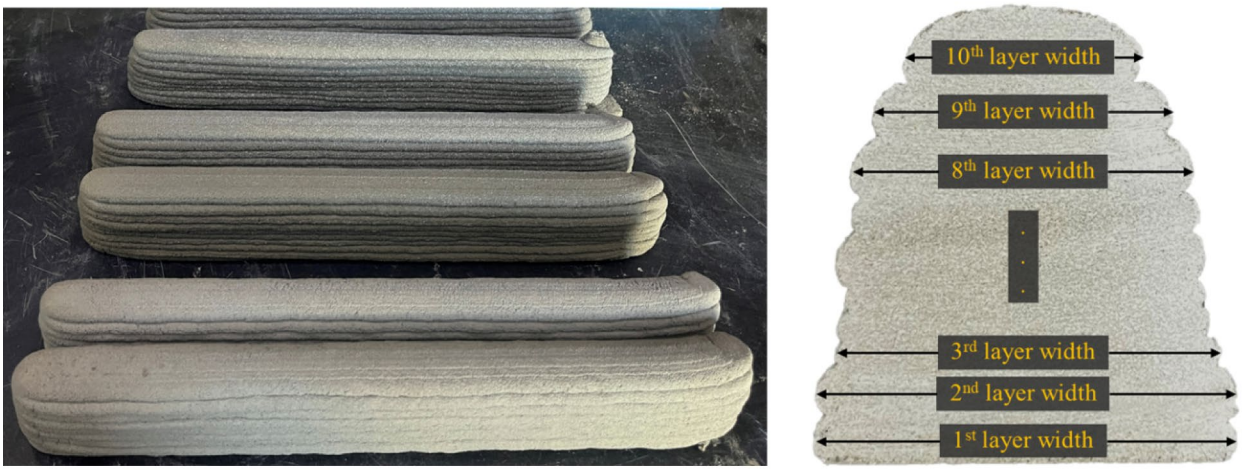


Fig. 5 (**a**) Printed samples and (**b**) corresponding cross sections used for layer deformation measurements

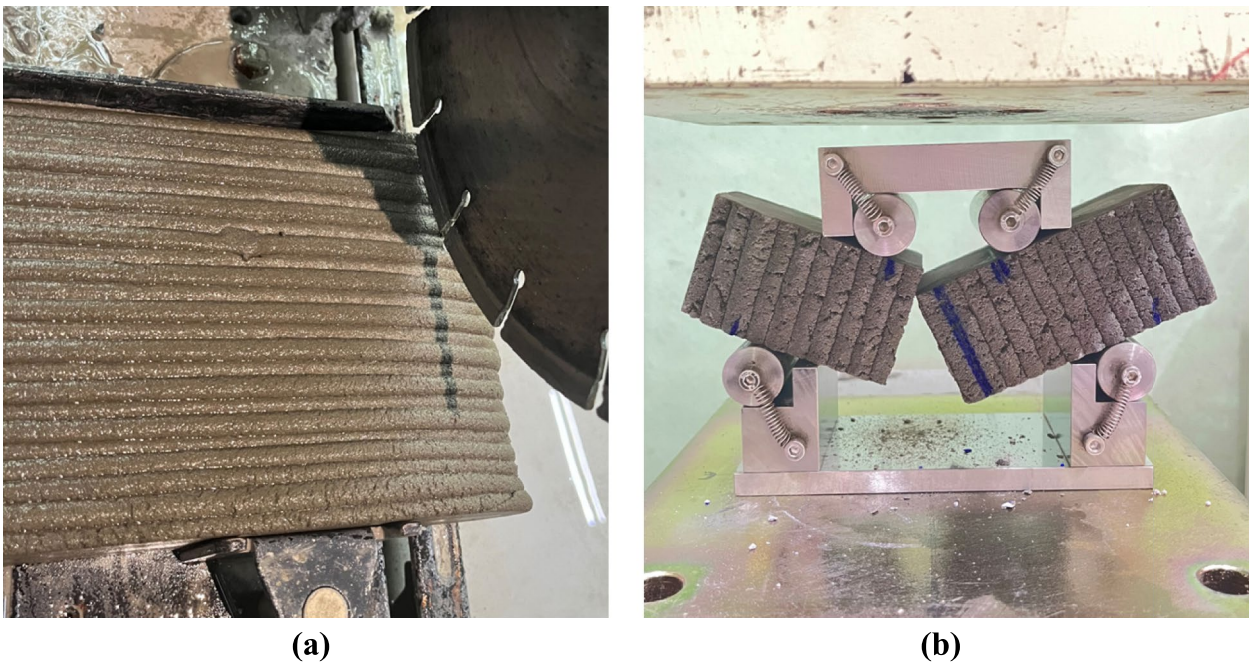


Fig. 6 (**a**) Preparation of the printed prism and (**b**) fractured prism after testing

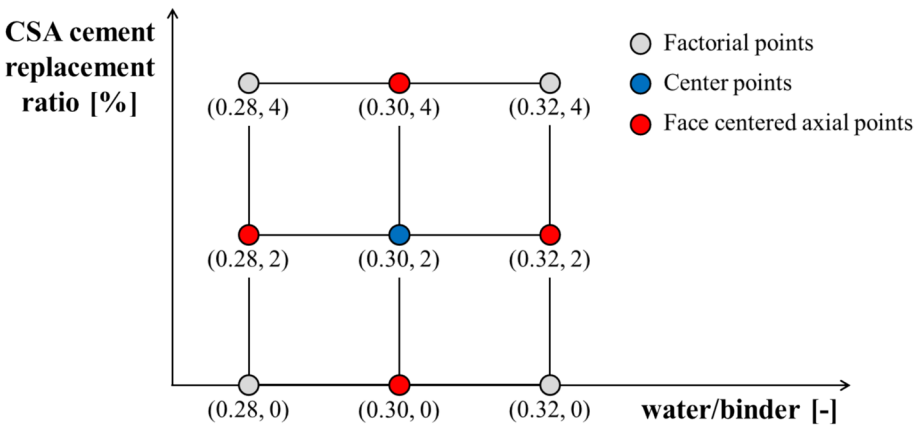


Fig. 7 CCF design with two explanatory variables

where *IBP* is the interlayer bonding performance [%], and $f_{r,printed}$ and $f_{r,cast}$ are the flexural strengths [MPa] of the printed and mold-cast prisms, respectively.

2.4 Statistical Optimization

Design of experiments (DOE) is a systematic approach to planning experiments, determining data collection procedures, and applying statistical techniques for analysis, all of which aim to solve problems efficiently (Montgomery, 2020; Mora & Moreno, 2021). This approach enables researchers to obtain maximum information while minimizing costs and time. In this study, layer strain and interlayer bonding performance were selected as the response variables, as they serve as key indicators of the buildability of 3DCP materials. A 3^2 factorial design (two explanatory variables at three levels each) was employed, with the water–binder ratio and CSA cement replacement ratio designated as the explanatory variables. These variables were chosen due to their intuitive and effective ability to control layer strain and interlayer bonding performance in 3DCP mixtures. A full factorial design was adopted to analyze both the main and interaction effects of these factors. From a practical standpoint, a central composite face-centered (CCF) design (Fig. 7)

was used, as the maximum CSA cement replacement ratio had already been constrained to ensure satisfactory extrudability and avoid overloading the printer. To compare the relative magnitudes of factor effects effectively, the variables were coded (Montgomery, 2020): water–binder ratios of 0.28, 0.30, and 0.32 were coded as −1, 0, and + 1, respectively, and CSA cement replacement ratios of 0%, 2%, and 4% were similarly coded as −1, 0, and + 1. A total of 13 printing experiments were conducted, with one experiment for each factorial and axial point and five repetitions at the central point. To ensure objectivity and minimize the influence of uncontrolled factors, the experimental run was randomized. For each printing batch, three printed specimens were produced, and at least three measurements were taken per specimen. Thus, each batch was represented by the mean value obtained from nine independent measurements.

To statistically evaluate the differences between groups, an analysis of variance (ANOVA) was conducted. ANOVA is a hypothesis testing method that uses the F-distribution to compare the variance within groups to the variance between groups, thereby identifying statistically significant differences (Oh et al., 2023; Tabachnick, 2007). Response surface methodology was then applied to investigate the relationship between multiple explanatory variables and the response variables. This approach combines mathematical and statistical techniques to model the response surface and determine the optimal response values (Myers et al., 2016; Subasi et al., 2016; Xie et al., 2021). In this study, a quadratic model was adopted to approximate the relationship between each response variable and the explanatory variables. The quadratic model is expressed in the following equation:

$$y = \beta_0 + \sum_{i=1}^{k} \beta_i x_i + \sum_{i=1}^{k} \beta_{ii} x_i^2 + \sum_{i<j}^{k} \beta_{ij} x_i x_j + \varepsilon \quad (3)$$

where y is the response variable, x_i and x_j are the explanatory variables, β_0 is the constant coefficient, β_i is the linear coefficient, and β_{ii} is the quadratic coefficient. The term β_{ij} represents the interaction coefficient between the explanatory variables, and ε is the error term.

Using the response surface model equations derived with the water–binder ratio and CSA cement replacement ratio as explanatory variables and layer strain and interlayer bonding performance as response variables, desirability functions were applied to determine the optimized mixture proportions. The objective was to minimize layer strain while maximizing interlayer bonding performance. The desirability function technique defines an individual desirability function, d_i, for each response variable, y_i, where $0 \le d_1 \le 1$; $d_i = 1$ when the target is achieved and $d_i = 0$ when the value is outside the acceptable range (Montgomery, 2020). For n response variables, the overall desirability (D) is calculated using Eq. (4), and the design variables that maximize D are identified as the optimal design variables:

$$D = (d_1 \cdot d_2 \cdots d_{n-1} \cdot d_n)^{\frac{1}{n}} \quad (4)$$

In this study, layer strain (y_1) was minimized and interlayer bonding performance (y_2) was maximized. The individual desirability functions d_1 and d_2 are defined by Eqs. (5) and (6), respectively, and the overall desirability (D) is calculated using Eq. (7):

$$d_1 = \begin{cases} 1 & y_1 < T_1 \\ \left(\dfrac{U_1 - y_1}{U_1 - T_1}\right)^{r_1} & T_1 \le y_1 \le U_1 \\ 0 & y_1 > U_1 \end{cases} \quad (5)$$

$$d_2 = \begin{cases} 0 & y_2 < L_2 \\ \left(\dfrac{y_2 - L_2}{T_2 - L_2}\right)^{r_2} & L_2 \le y_2 \le T_2 \\ 1 & y_2 > T_2 \end{cases} \quad (6)$$

$$D = (d_1 \cdot d_2)^{\frac{1}{2}} \quad (7)$$

where T_1 and T_2 are the target values for y_1 and y_2; U_1 is the upper limit of y_1; L_2 is the lower limit of y_2; and r_1 and r_2 are the weights assigned to each desirability function.

3 Results and Discussion

3.1 Material Experiments

Figure 8 shows the fluidity of the mixtures as a function of the CSA cement replacement ratio. The average flow value for the group with a water–binder ratio of 0.32 was used as the reference, and the average flows for the 0.30 and 0.28 groups were 93.1% and 82.9%, respectively. These results indicate a clear decrease in fluidity as the water–binder ratio decreases. Conversely, changes in fluidity with respect to the CSA cement replacement ratio did not exhibit a distinct trend across all groups. However, a noticeable reduction in fluidity was observed in the 0.28 water–binder ratio group as the CSA cement replacement ratio increased compared with the other mixtures. This behavior suggests that while small amounts of CSA cement replacement have limited influence on early age fresh-state properties when sufficient free water is available, the effects become more pronounced under conditions with restricted free water. This result can be attributed to the rapid initial hydration reaction of the CSA cement, which is consistent with previous findings (Hung et al., 2024; Jiang et al., 2022). Given that the very early fresh-state properties of the material

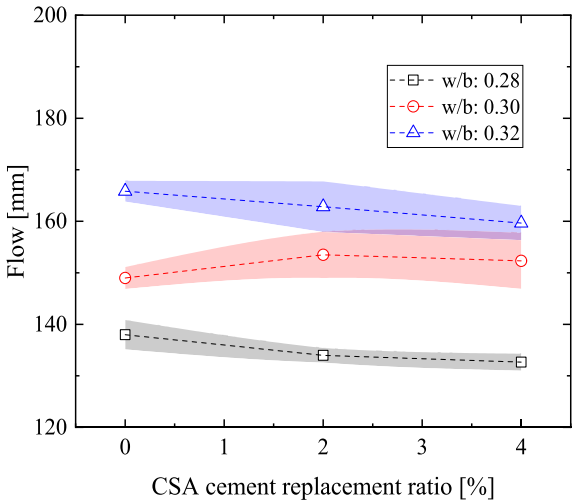


Fig. 8 Fluidity of fresh specimens as a function of the CSA cement replacement ratio

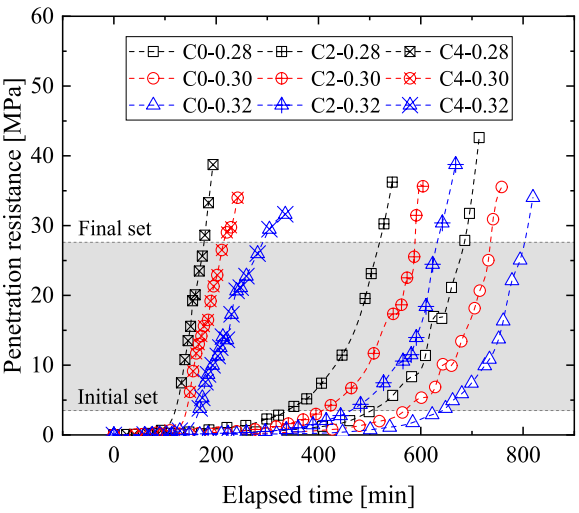


Fig. 9 Penetration resistance test results for each specimen

directly influence layer deformation during 3D printing, increasing the CSA cement replacement ratio is expected to effectively reduce layer deformation, particularly at lower water–binder ratios.

Figure 9 presents the penetration resistance results for each specimen, and Table 3 summarizes the corresponding initial and final setting times at penetration resistances of 3.5 and 27.6 MPa, respectively. The specimen with the fastest setting behavior was C4-0.28, with initial and final setting times of 109 and 176 min, respectively. In contrast, the slowest setting specimen was C0-0.32, which exhibited initial and final setting times of 639 and 801 min, respectively. Within each water–binder ratio group, the setting time decreased as the CSA cement replacement ratio increased. For the 0.28 water–binder ratio group, increasing the CSA cement replacement ratio from 0% to 2% and from 2% to 4% resulted in average reductions of 28.5% and 66.8% in the initial and final setting times, respectively. The corresponding reduction rates were 24.3% and 65.7% for the 0.30 group and 24.4% and 59.1% for the 0.32 group, respectively. These results indicate that the reduction in setting time becomes more pronounced at lower water–binder ratios. Furthermore, the decrease in setting time was greater when the CSA cement replacement ratio increased from 2% to 4% than when it increased from 0% to 2%, suggesting a nonlinear relationship between CSA cement replacement and setting time reduction. This trend is likely associated with the reduced particle spacing at lower water–binder ratios, which accelerates hydrate formation, consistent with previous findings (Burris & Kurtis, 2022; Gołaszewska et al., 2024). In addition, the nonlinear increase in the setting time reduction effect may be attributed to the rapid formation of AFm phases such as monosulfoaluminate when calcium sulfate becomes insufficient beyond a critical replacement level (Park et al., 2021). When comparing changes in setting time across water–binder ratios, the average increases in initial and final setting times from 0.28 to 0.30 were 10.3%, 16.9%, and 20.6% for the 0%, 2%, and 4% CSA cement replacement groups, respectively. Similarly, when the water–binder ratio increased from 0.30 to 0.32, the average increase in setting time was 10.6%, 10.4%, and 30.8% for the 0%, 2%, and 4% CSA groups, respectively. These results demonstrate that the CSA cement replacement ratio is a more influential factor affecting setting time than the water–binder ratio, and its effect becomes substantially stronger once a critical replacement ratio is exceeded. Furthermore, the influence of CSA cement on the setting time increases as the water–binder ratio decreases.

Table 3 Initial and final setting times for each specimen

Specimen ID	Initial setting time [min]	Final setting time [min]
C0-0.28	502	685
C2-0.28	338	519
C4-0.28	109	176
C0-0.30	569	736
C2-0.30	406	588
C4-0.30	130	215
C0-0.32	639	801
C2-0.32	460	633
C4-0.32	164	292

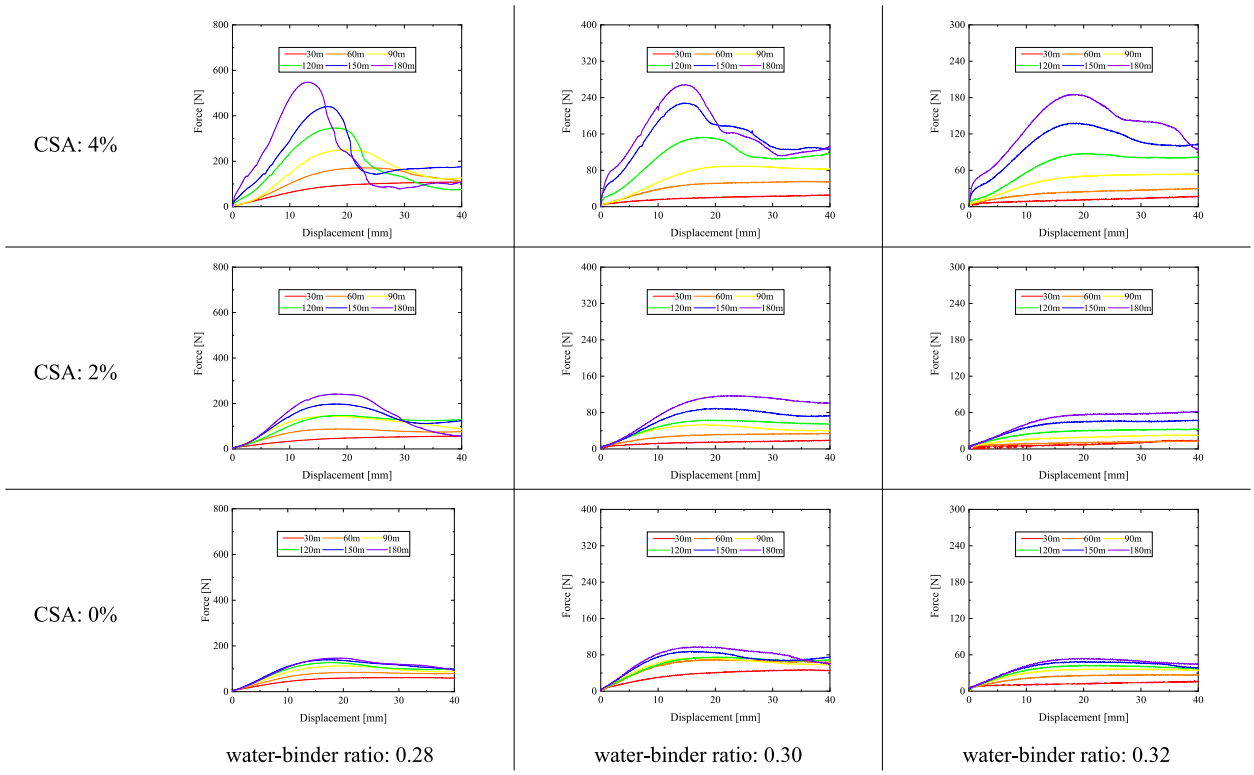


Fig. 10 Force–displacement curves for each specimen

Table 4 Peak forces for each specimen at various times after water–binder contact

Specimen ID	Peak force [N]					
	30 min	60 min	90 min	120 min	150 min	180 min
C0-0.28	62.6	85.4	113.4	128.2	140.4	147.6
C2-0.28	57.0	88.6	145.4	148.6	198.8	242.2
C4-0.28	109.4	171.8	250.8	347.0	441.2	548.0
C0-0.30	47.6	71.0	74.6	75.4	88.0	98.2
C2-0.30	19.6	34.4	54.0	64.0	89.6	117.6
C4-0.30	26.4	56.4	90.0	153.0	228.4	268.6
C0-0.32	17.2	28.0	37.4	43.4	49.4	54.4
C2-0.32	14.6	13.8	23.6	33.6	48.4	62.4
C4-0.32	17.8	30.8	54.6	88.2	138.2	185.6

Figure 10 presents the force–displacement curves obtained from the green strength tests, and Table 4 summarizes the corresponding peak forces measured at various elapsed times after initial water–binder contact. The green strength of all specimens increased with time and generally increased with higher CSA cement replacement ratios and lower water–binder ratios. Furthermore, the influence of CSA cement replacement on green strength became more pronounced as the water–binder ratio decreased. For the 0.32 water–binder ratio group, a 2% CSA cement replacement resulted in a noticeable increase in green strength compared to the 0% replacement only after 180 min, whereas the 4% replacement exhibited a meaningful increase starting at 120 min. In the 0.30 group, the 2% replacement ratio led to a noticeable improvement beginning at 150 min, while the 4% replacement ratio showed an increase at 90 min. In the 0.28 group, a 2% replacement produced a significant increase in green strength at 90 min, and 4% replacement ratio exhibited improvements as early as 30 min.

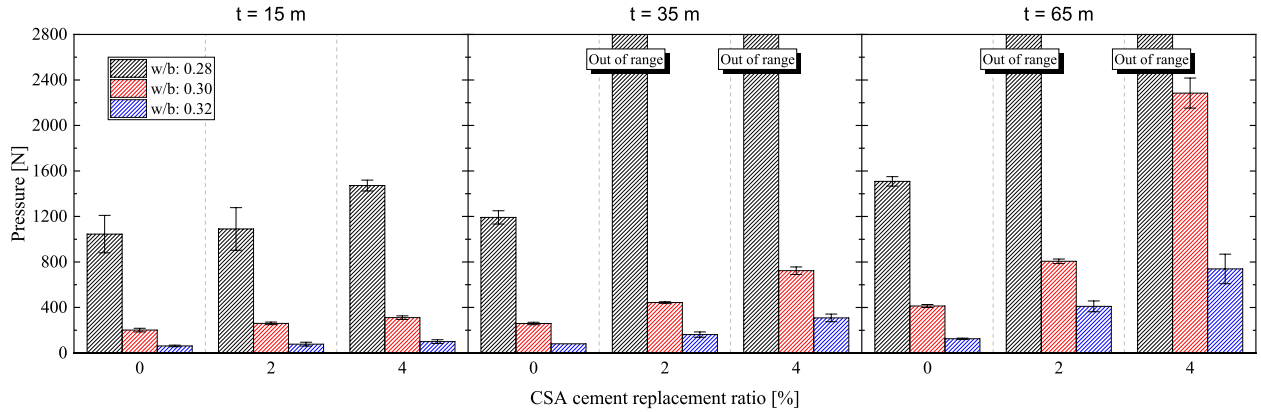


Fig. 11 Extrusion pressure as a function of the CSA cement replacement ratio

These results, considered alongside the fluidity trends in Fig. 8, indicate that CSA cement replacement provides a synergistic effect at lower water–binder ratios, effectively improving early age structural stability even at small replacement levels. Among all specimens, the lowest peak forces were observed for C0-0.32, with values of 17.2, 28.0, 37.4, 43.4, 49.4, and 54.4 N at 30, 60, 90, 120, 150, and 180 min, respectively. In contrast, the highest peak forces were recorded for C4-0.28, with values of 109.4, 171.8, 250.8, 347.0, 441.2, and 548.0 N at the same time intervals, representing increases of 636.0%, 613.6%, 670.6%, 799.5%, 893.1%, and 1007.4% compared with C0-0.32.

Figure 11 shows the extrusion pressure as a function of the CSA cement replacement ratio. From a 3DCP perspective, extrudability is a prerequisite for buildability, as smooth and continuous extrusion is essential for successful printing. Irregular or insufficient extrusion can interrupt the printing process and lead to pipe blockage or equipment malfunction in severe cases (Oh et al., 2021). Therefore, maintaining sufficient open time to ensure stable extrusion is critical. As shown in Fig. 11, extrusion pressure increased progressively with elapsed time due to structural build-up within the cement-based material (Oh & Choi, 2023; Reiter et al., 2018). In addition, the extrusion pressure increased with higher CSA cement replacement ratios. In the 0.28 water–binder ratio group, the specimen without CSA replacement exhibited increases in extrusion pressure of 14.1% and 44.4% at 35 and 65 min, respectively, relative to the pressure at 15 min. However, for the specimens with CSA cement replacement ratios of 2% and 4%, continuous extrusion could no longer be maintained after 35 min, because the required pressure exceeded the measurement range. In the 0.30 group, the extrusion pressures at 65 min for specimens with CSA cement replacement ratios of 0%, 2%, and 4% were 105.2%, 209.9%, and 635.7% of the corresponding pressures at 15 min, respectively.

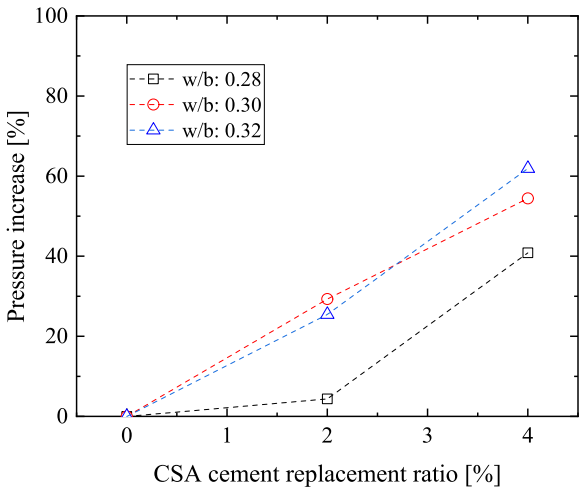


Fig. 12 Percentage increase in extrusion pressure relative to the CSA cement replacement ratio, calculated relative to the pressure of the 0% replacement specimen within each water–binder ratio group

Similarly, in the 0.32 group, the extrusion pressures for specimens with CSA cement replacement ratios of 0%, 2%, and 4% at 65 min were 102.4%, 428.4%, and 638.7% of the 15 min values. These results indicate that within each water–binder ratio group, the relative increase in extrusion pressure with time becomes more pronounced as the CSA cement replacement ratio increases. Figure 12 further illustrates the increase in extrusion pressure associated with higher CSA cement replacement ratios within each water–binder ratio group at 15 min after initial mixing. When compared with the green strength trends shown in Fig. 10, which primarily reflect material stiffness, the extrusion pressure results more distinctly captured the reduction in printability associated with CSA cement replacement. This difference arises, because the

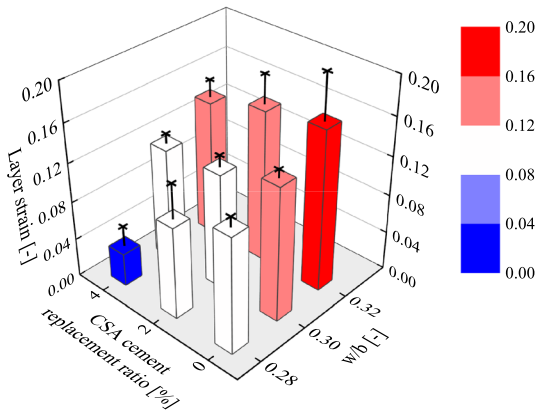


Fig. 13 Layer strain values for each specimen

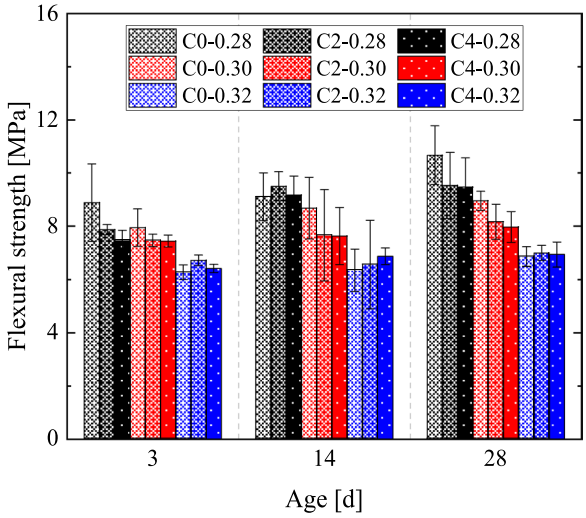


Fig. 14 Flexural strength of the cast prisms for each specimen at different curing ages

extrusion performance is significantly influenced not only by the yield stress of the material but also by its viscosity, with the CSA cement replacement increasing the viscosity and thereby affecting the extrusion behavior (Ke et al., 2020; Mechtcherine et al., 2020).

3.2 Printing Experiments

Figure 13 shows the layer strain value for each specimen. The layer strain decreased with increasing CSA cement replacement ratio and decreasing water–binder ratio. On average, the layer strain was reduced by 12.1% and 31.4% in the 2% and 4% CSA replacement groups, respectively, compared with that in the 0% group. Similarly, the average layer strain decreased by 19.4% and 46.2% in the 0.30 and 0.28 water–binder ratio groups, respectively, compared with the 0.32 group. These results indicate that changes of 2% in CSA cement replacement and 0.02 in the water–binder ratio have a substantial effect on layer strain. A particularly pronounced reduction was observed in the 0.28 water–binder ratio group, where layer strain decreased by 20.3% and 71.3% for the 2% and 4% CSA cement replacement ratios, respectively, relative to the 0% group. In contrast, the effect of CSA cement replacement on layer strain was less significant in groups with water–binder ratios of 0.30 or higher. Specifically, reductions of 13.3% and 15.8% were observed in the 0.30 group, and reductions of 5.1% and 15.5% were observed in the 0.32 group for the 2% and 4% CSA cement replacement ratios, respectively. This trend is consistent with the synergistic effect of CSA cement at lower water–binder ratios, as discussed in Sect. 3.1. Reducing layer strain is generally beneficial from a 3DCP perspective, as it improves shape stability during printing. However, excessive reduction in layer strain may also shorten the open time and weaken the interlayer bonding performance. Therefore, an appropriate tolerance range for layer strain must be defined based on the target structural dimensions or the desired extruded layer width.

Figure 14 presents the flexural strength of the cast prisms for each specimen as a function of curing age. As the curing age increased from 3 to 14 to 28 days, the average flexural strength of the 0.28 water–binder ratio group increased by 14.6% and 22.4%, respectively. Similarly, the 0.30 group showed increases of 4.9% and 9.8%, respectively, while the 0.32 group exhibited increases of 2.0% and 7.2%, respectively. At 3 days, the average flexural strengths of the 0.30 and 0.32 groups were 94.3% and 80.0% of the 0.28 group, respectively. These values decreased to 86.3% and 71.2% after 14 days and 84.6% and 70.1% at 28 days, respectively. These results confirm a typical increase in flexural strength with curing time across all specimens, with greater strength gains and higher strength values observed at lower water–binder ratios. The CSA cement replacement ratio did not exhibit a clear trend in its effect on the rate of strength gain over time; however, the flexural strength decreased as the CSA cement replacement ratio increased. At 3 days, the average flexural strengths of the 2% and 4% CSA replacement groups were 95.4% and 92.4% of the 0% group, respectively. At 14 days, the corresponding values were 98.3% and 98.0%, and at 28 days, they were 93.2% and 92.0%. This behavior is consistent with previous findings (Wang et al., 2024; Wolf et al., 2021), which suggest that while increasing the CSA cement replacement ratio promotes the formation of ettringite, the mechanical strength may decrease due to insufficient gel formation to fill the voids between ettringite (Trauchessec et al., 2015; Yang et al.,

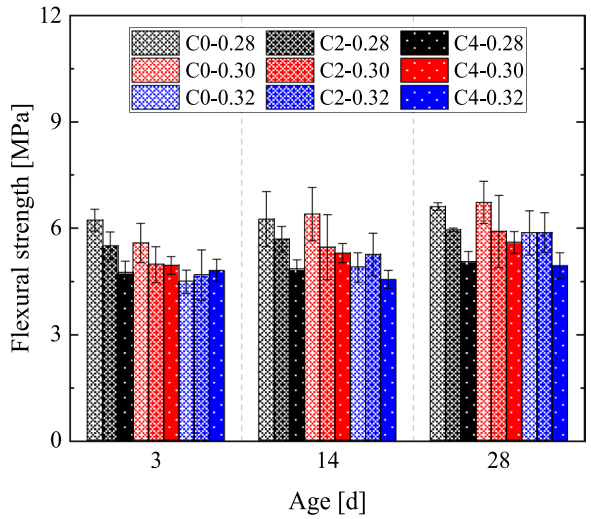


Fig. 15 Flexural strength of printed prisms for each specimen at different curing ages

2021). Additional microstructural analysis is required to further clarify this mechanism.

Figure 15 presents the flexural strength of the printed prisms for each specimen as a function of curing age. Unlike the trends observed for the cast prisms in Fig. 14, no distinct trend was identified with respect to the water–binder ratio. The average 3-day flexural strengths of the 2% and 4% CSA replacement groups were 92.9% and 89.0% of the 0% group, respectively. At 14 days, the corresponding values were 93.5% and 83.8%, and at 28 days, they were 92.4% and 81.2%, respectively. These results indicate that the influence of CSA cement replacement was more pronounced in the printed prisms than in the cast prisms. Printed prisms which are produced through additive layering exhibit a higher degree of microstructural variability than cast prisms. This variability is likely associated with changes, such as the formation of larger voids and variations in void morphology (Yu et al., 2021). In addition, surface moisture plays a critical role in interlayer bonding performance (Moelich et al., 2021). In mixtures containing CSA cement, the rapid early hydration reactions may reduce surface moisture, thereby intensifying the sensitivity of printed specimens to CSA replacement. As a result, the effect of CSA cement replacement on the flexural strength of the printed prism appears more pronounced than that observed in the cast prism in Fig. 14.

Figure 16 presents the interlayer bonding performance of the specimens after 3, 14, and 28 days. At all ages, the interlayer bonding performance increased with higher water–binder ratios and lower CSA cement replacement ratios. At 3 days, the 0.28 group exhibited an average

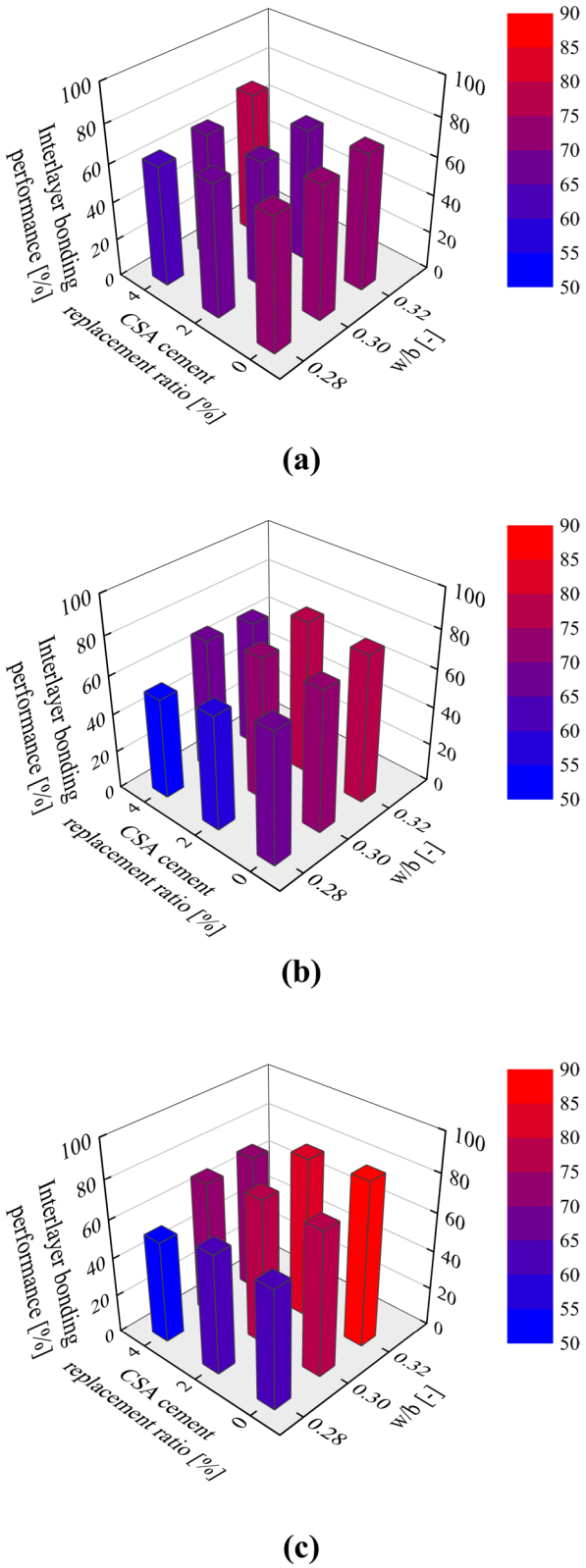


Fig. 16 Interlayer bonding performance of each specimen at different curing ages: (**a**) 3 days; (**b**) 14 days; and (**c**) 28 days

interlayer bonding performance of 67.8%, compared with 67.9% and 72.1% for the 0.30 and 0.32 groups, representing increases of 0.1% and 6.4%, respectively. At 14 days, the 0.28 group exhibited an average value of 60.5%, whereas the 0.30 and 0.32 groups increased by 19.9% (72.5%) and 23.2% (74.5%), respectively. By 28 days, the average interlayer bonding performance of the 0.28 group was 59.2%, whereas that of the 0.30 and 0.32 groups increased by 24.3% (73.6%) and 35.1% (80.0%), respectively. Regarding CSA cement replacement, the 3-day interlayer bonding performance of the 2% and 4% replacement groups decreased by 2.8% and 3.4%, respectively, relative to the 0% group (70.7%). At 14 days, the decreases were 2.3% (71.5%) and 14.0% (62.9%), and at 28 days, they were 0.5% (73.8%) and 12.5% (64.9%), respectively, relative to the 0% group (74.2%). These findings indicate that the effects of the water–binder ratio and CSA cement replacement ratio on interlayer bonding performance became more pronounced with longer curing time. This trend is likely due to the progressive filling of microscopic voids by hydrates during hydration, while larger, irregularly shaped, and continuous voids in the interlayers of printed prisms persist as defects, significantly affecting interlayer bonding during flexural testing (Yu et al., 2021; Zhang et al., 2022). At all ages, the C4-0.28 specimens exhibited substantially reduced interlayer bonding performance due to the combination of a low water–binder ratio and a high CSA cement replacement ratio. However, the C0-0.32 specimens, which were expected to show the highest interlayer bonding performance, did not consistently exhibit the highest values. This discrepancy may be attributed to the water solubility of VMA, which has a stronger effect in mixtures containing abundant free water. Under these conditions, the VMA increases viscosity, promotes air entrainment, and leads to the formation of macroscopic voids, thereby reducing the interlayer bonding performance (Bhattacherjee et al., 2024; Wang et al., 2022a, 2022b; Xie et al., 2023). These defects, distributed both within the interlayer plane and throughout the prism, significantly decrease the flexural strength of the printed elements. Figure 17 displays the defects associated with air entrainment observed in the 0.32 group. Consequently, the flexural strength of the printed prisms in the 0.32 group may have been underestimated due to the additional effects of VMA. This effect may also depend on printing parameters, such as pump pressure and print speed. Future research could address this issue by minimizing parameter-induced variability and employing alternative testing methods to directly evaluate interlayer bonding.

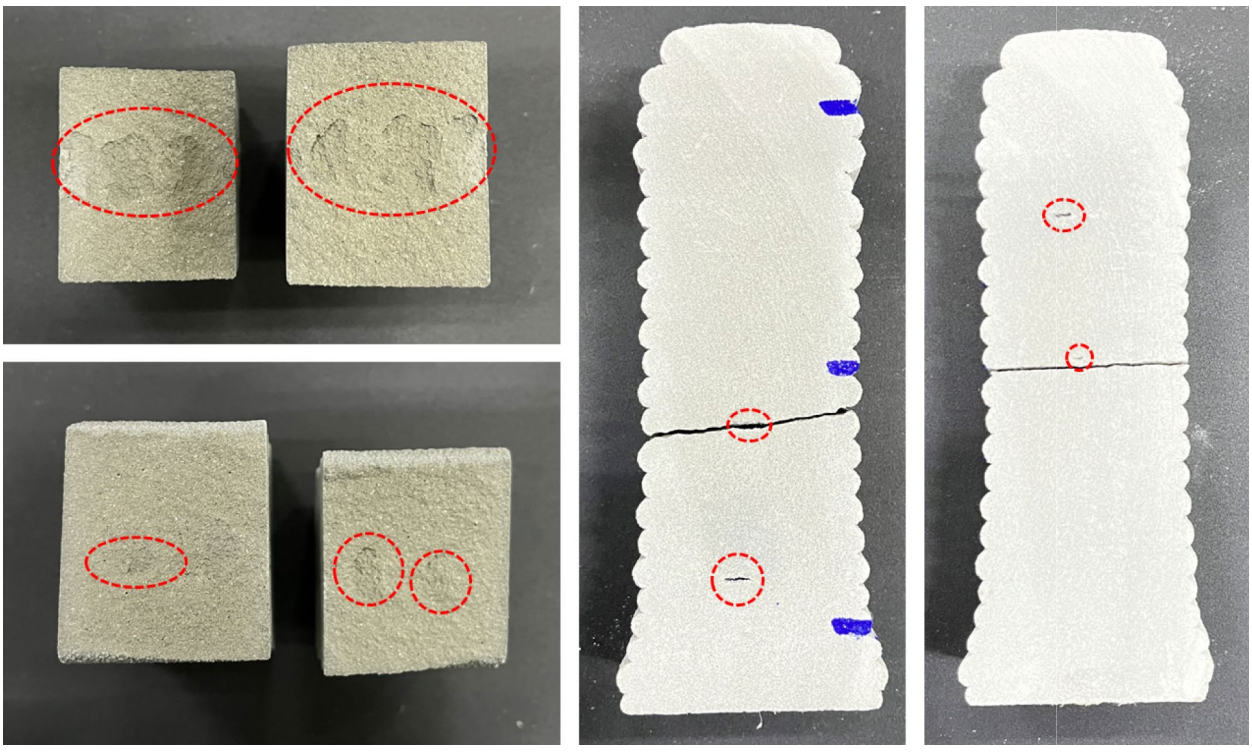


Fig. 17 Defects in printed prisms with a water–binder ratio of 0.32: (**a**) fracture surfaces and (**b**) cut cross sections (red circles indicate defect areas)

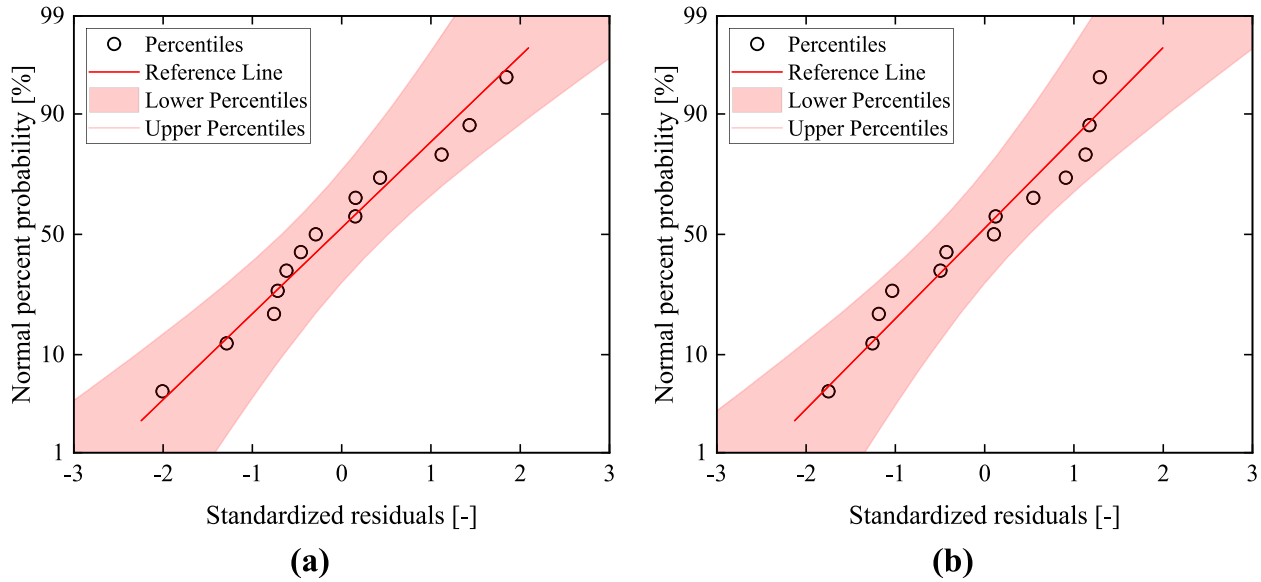


Fig. 18 Normal probability plots of standardized residuals with 95% confidence intervals: (**a**) layer strain and (**b**) interlayer bonding performance

Table 5 ANOVA results for the experimental data

Response variables	Source	DF [1]	Adj SS [2]	Adj MS [3]	F ratio	*p* value
y_1 [4]	x_1 [6]	1	0.007695	0.007695	60.92	**< 0.001**
	x_2 [7]	1	0.002956	0.002956	23.40	**< 0.001**
	x_1 [6] * x_2 [7]	1	0.000896	0.000896	7.091	**0.026**
	Lack of fit	5	0.000729	0.000146	1.431	0.375
	Pure error	4	0.000408	0.000102		
	Total	12	0.012683			
y_2 [5]	x_1 [6]	1	649.82	649.82	24.88	**< 0.001**
	x_2 [7]	1	128.40	128.40	4.917	0.051
	Lack of fit	6	149.87	24.978	0.898	0.569
	Pure error	4	111.29	27.824		
	Total	12				

[1] Degree of freedom. [2]Adjusted sums of squares. [3]Adjusted mean square. [4]Layer strain. [5]Interlayer bonding performance (28 days). [6]Water–binder ratio. [7]CSA cement replacement ratio

3.3 Statistical Analysis

Statistical analysis and mixture optimization were conducted using the results from the 13 printing experiments described in Sect. 2.4. For the response variable representing interlayer bonding performance, the analysis focused on the 28-day data, where the effect of mixture composition was most clearly observed.

Figure 18 shows the normal probability plots of the standardized residuals for each response variable. All standardized residual values were within the 95% confidence interval, indicating the absence of statistically significant outliers. Furthermore, the response values closely followed a linear trend, confirming that the residuals were normally distributed (Montgomery & Runger, 2020).

Table 5 summarizes the ANOVA results for the experimental data, conducted at a significance level (α) of 0.05 (95% confidence level). The null hypothesis is not rejected when the p value exceeds 0.05, indicating that the explanatory variable does not have a statistically significant effect on the response variable. Conversely, the alternative hypothesis is accepted when the p value is less than or equal to 0.05, confirming statistical significance (Montgomery & Runger, 2020; Tabachnick, 2007). Higher order terms that were not statistically significant and did not meaningfully contribute to the model were pooled

as the error term. For layer strain, the quadratic terms $x_1 * x_1$ and $x_2 * x_2$ were excluded, whereas for interlayer bonding performance, the interaction term $x_1 * x_2$ and both quadratic terms were excluded. The water–binder ratio was statistically significant for both response variables. The CSA cement replacement ratio was statistically significant for layer strain but not for interlayer bonding performance at the 95% confidence level. However, the p value associated with the CSA cement replacement ratio in the interlayer bonding analysis was close to 0.05, despite the relatively small 2% increment between factor levels. This suggests that the CSA cement replacement ratio may still have a practically meaningful influence on interlayer bonding performance, particularly in mixture proportioning for 3DCP. Therefore, its inclusion in the regression model is justified. Furthermore, the p values for lack of fit in all ANOVA results exceeded 0.05, indicating that the terms pooled into the error term were unlikely to have a statistically significant effect on the response variables. The interaction between the water–binder ratio and CSA cement replacement ratio exhibited a statistically significant effect on layer strain, confirming the synergistic behavior associated with decreasing the water–binder ratio while increasing the CSA cement replacement ratio (Fig. 13). Figure 19 presents the Pareto charts for each response variable, where factors that exceed the vertical red line, representing the statistical significance threshold, are considered significant (Mora & Moreno, 2021). These results are consistent with the ANOVA results.

Equations (8) and (9) present the statistical models obtained by substituting the significant terms identified through ANOVA into Eq. (3). The p values for both models were less than 0.001, indicating high statistical significance. The coefficients of determination R^2, adjusted R^2, and predicted R^2 for Eq. (8) were 0.9104, 0.8805, and 0.7228, respectively, while those for Eq. (9) were 0.7481, 0.6985, and 0.5540, respectively. These values confirm that the regression equations have acceptable explanatory power (Hou et al., 2020; Mora & Moreno, 2021). The relatively lower R^2 values for the interlayer bonding performance model compared with the layer strain model are attributed to the inherent differences in the factors governing the two responses. Layer strain is primarily controlled by rheological properties, such as yield stress and plastic viscosity, under fixed printing conditions, which can be directly and quantitatively linked to mixture composition (Buswell et al., 2018; Muthukrishnan et al., 2021). In contrast, the interlayer bonding performance, assessed using a four-point bending test, may exhibit greater variability, because the crack propagation path does not necessarily follow the interlayer interface and may instead depend on internal defect distribution and loading configuration, as shown in Fig. 17. Furthermore, variations in curing efficiency, pore structure, and spatial heterogeneity of hydration products may introduce additional uncertainty (Babafemi et al., 2021; Moelich et al., 2021; Wang et al., 2020), resulting in a lower model correlation for interlayer bonding performance:

$$y_1 = 0.12048 + 0.03581x_1 - 0.02220x_2 + 0.01496x_1x_2 \tag{8}$$

$$y_2 = 72.39 + 10.41x_1 - 4.63x_2 \tag{9}$$

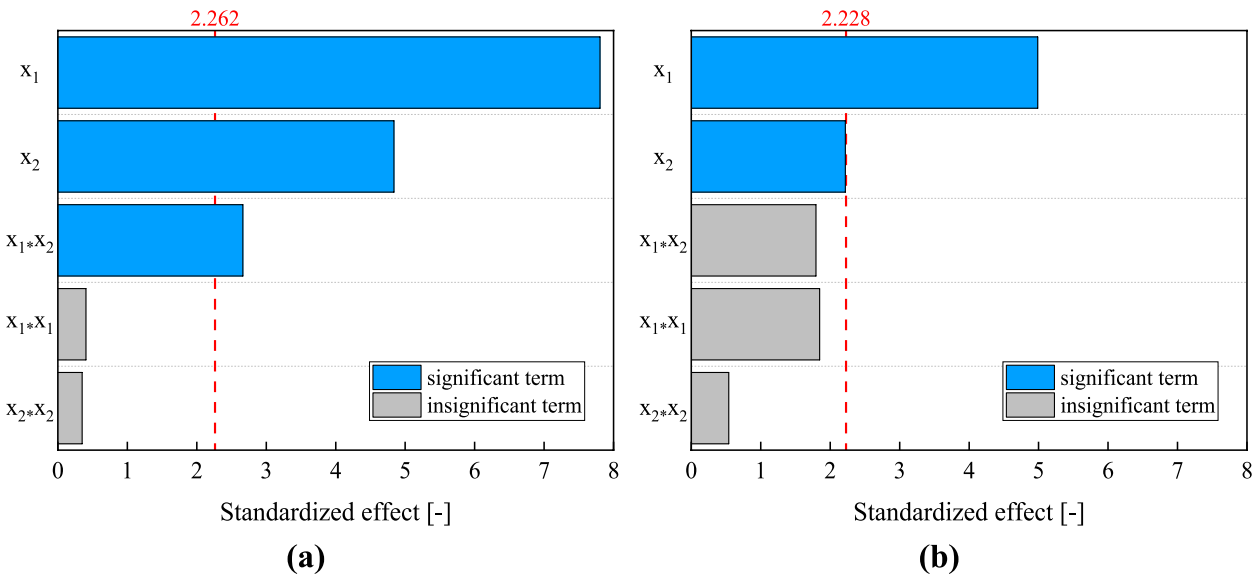


Fig. 19 Pareto charts of standardized effects: (**a**) layer strain and (**b**) interlayer bonding performance

Table 6 Experimental design with coded levels for the explanatory variables and their corresponding response values

Run	Explanatory variables (Coded units)		Response variables			
			Actual values		Predicted values	
	x_1[1]	x_2[2]	y_1[3] [-]	y_2[4] [%]	y_1[3] [-]	y_2[4] [%]
1	−1	+1	0.03436	53.292	0.04751	57.353
2	+1	+1	0.14063	71.310	0.14906	78.167
3	0	0	0.12215	77.939	0.12048	72.386
4	0	0	0.13596	78.727	0.12048	72.386
5	−1	0	0.09562	62.445	0.08467	61.979
6	0	−1	0.13824	75.113	0.14268	77.012
7	−1	−1	0.11994	61.954	0.12183	66.605
8	0	+1	0.11633	70.190	0.09828	67.760
9	+1	−1	0.16635	85.481	0.16352	87.419
10	+1	0	0.15781	83.341	0.15629	82.793
11	0	0	0.11230	78.152	0.12048	72.386
12	0	0	0.11381	76.851	0.12048	72.386
13	0	0	0.11275	66.221	0.12048	72.386

[1] Water–binder ratio. [2] CSA cement replacement ratio. [3] Layer strain. [4] Interlayer bonding performance (28 days)

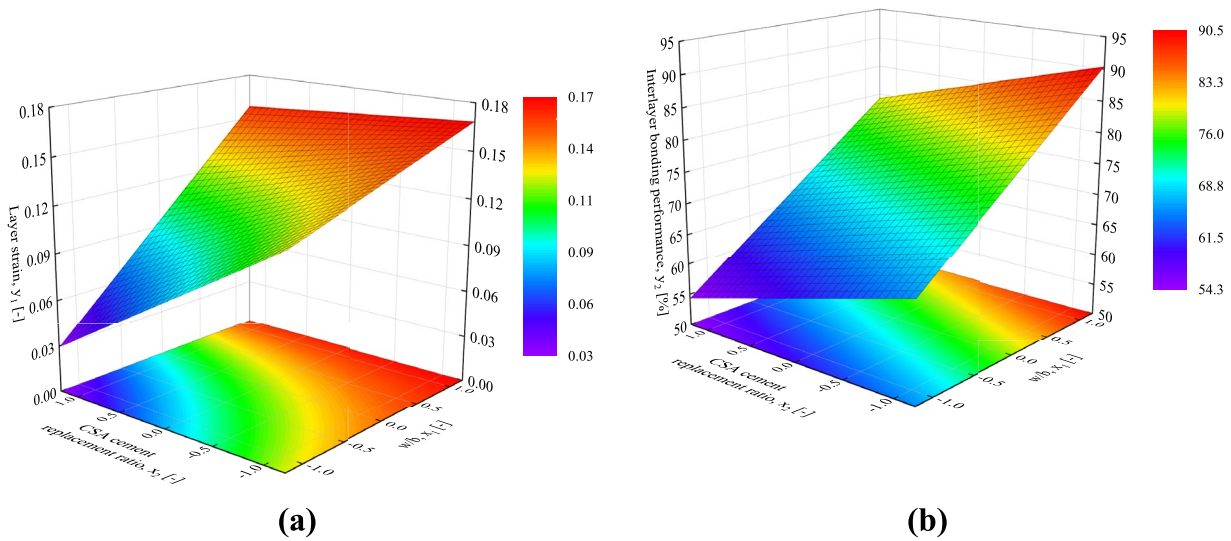


Fig. 20. 3D response surface plots for (**a**) layer strain and (**b**) interlayer bonding performance

Table 6 presents the experimental design, the measured response values, and the predicted values calculated using Eqs. (8) and (9). The close agreement between the measured and predicted values demonstrates the validity of the models. Figure 20 shows the response surface plots for the two response variables, with the water–binder ratio and CSA cement replacement ratio as the explanatory variables. The response surfaces exhibited no stationary points, instead showing an increasing trend with higher water–binder ratios and lower CSA cement replacement ratios. However, the slopes differed in magnitude, indicating varying sensitivities of the response variables to these factors.

3.4 Verification of Optimization

Based on the analysis in Sect. 3.3, this section verifies the optimized mixture aimed at minimizing layer strain and maximizing interlayer bonding performance. The optimal values were determined using Eqs. (5, 6, 7) in Sect. 2.4, and Table 7 summarizes the results of the statistical optimization. The conversion of the coded values to actual engineering units yielded a water–binder ratio of 0.297

Table 7 Results of statistical optimization

Determined explanatory variables		Optimized response variables				Desirability
		Predicted values		Actual values		
x_1 [1]	x_2 [2]	y_1 [3] [-]	y_2 [4] [%]	y_1 [3] [-]	y_2 [4] [%]	
–0.13131	0.93939	0.09308	66.8434	0.08638	62.2741	0.48344

[1] Water–binder ratio. [2]CSA cement replacement ratio. [3] Layer strain. [4] Interlayer bonding performance (28 days)

and a CSA cement replacement ratio of 3.88%. Under these conditions, the predicted layer strain and interlayer bonding performance were 0.09308% and 66.8434%, respectively, with corresponding individual desirability values of 0.55513 and 0.42100. The optimized mixture proportions were then experimentally implemented, and the 28-day interlayer bonding performance was measured following the procedures described in Sect. 2.3. Each result represents the average of three specimens. The measured layer strain was 0.08638, corresponding to a relative error of 7.76% compared with the predicted value. The measured interlayer bonding performance was 62.2741%, with a relative error of 7.34%. Consequently, the mean relative error (MRE) for the model, calculated using both response variables was 7.55%. These results demonstrate that the statistical model provides reasonable predictive accuracy and is practically applicable. Furthermore, the optimized mixture exhibited improved layer strain and interlayer bonding performance relative to other tested mixtures, confirming the validity of the optimized mixture design.

4 Limitations and Pathways

Despite the effectiveness of the optimization approach used in this study, several limitations and remaining challenges should be addressed in future research. From a material standpoint, the ranges of the CSA cement replacement ratio and water–binder ratio were selected based on the printable window under fixed experimental conditions, including the characteristics of the raw materials, aggregate-to-binder ratio, admixture type and dosage, target printed geometry, and the performance and parameters of the printing equipment. Therefore, the ranges investigated in this study represent a stable printable window specific to the current material system and printing configuration. Under different mixture designs or printing conditions, the applicable ranges and quantitative effects of the CSA cement replacement ratio and water–binder ratio may vary. Future work should expand the variables and explore a broader spectrum of mixture and printing conditions to enhance generalizability.

In terms of experimental evaluation, flowability was assessed using simple comparative measurements to capture general trends among mixtures. Although this approach was effective for the assessment of printability, it did not provide detailed quantification of key rheological properties, such as static and dynamic yield stress, plastic viscosity, and thixotropic structural build-up. Future studies should incorporate more comprehensive rheological analyses to deepen the mechanistic understanding of the fresh-state behavior in mixtures incorporating CSA cement. Similarly, from a statistical and optimization perspective, the predictive model was developed using a limited number of experimental runs and variables, which constrained its robustness and extrapolation capacity. Additional parameters influencing layer strain and interlayer bonding performance should be considered to improve model reliability and applicability.

Furthermore, replacing a portion of OPC with CSA cement alters the hydration product assemblage, which may affect long-term properties, such as shrinkage and durability. Previous studies have shown that CSA-based binders may exhibit different shrinkage behaviors due to rapid hydration kinetics, expansive ettringite formation, and variations in self-desiccation during hardening (Ke et al., 2022; Sirtoli et al., 2020), and generally show improved sulfate resistance due to lower C_3A content and early ettringite stabilization (Bescher et al., 2016). In this study, the CSA cement was a rapid-hardening, ye'elimite-rich type used at a replacement level below 5%, and the long-term chemical effects are expected to be limited under the current conditions. However, the potential effects of shrinkage, moisture exchange, and environmental exposure on interlayer bonding and durability require further investigation, because 3D-printed layers are directly exposed to ambient environments.

Overall, this study demonstrated that partial binder replacement (< 5%) combined with moderate adjustment of the water–binder ratio can effectively enhance the printability and buildability of 3D printable cement-based materials. The use of a DOE-based experimental framework and subsequent verification confirmed the practical feasibility of the proposed optimization approach, suggesting its suitability for efficient implementation in real 3D printing applications. Academically, the results validate the applicability of the statistical optimization

framework to 3DCP systems and provide a foundational reference for future development of mix design optimization strategies for 3D printable materials.

5 Conclusions

This study investigated the time-dependent fresh-state properties and buildability-related characteristics of 3DCP materials, with a focus on printed layer deformation and interlayer bonding performance. The water–binder ratio and CSA cement replacement ratio were used as explanatory variables, while layer strain and interlayer bonding performance were analyzed as response variables to determine the optimal mixture proportions. The key findings are as follows:

1. Incremental increases of 2% in the CSA cement replacement ratio had a relatively modest effect on very early fresh-state behavior compared with a 0.02 decrease in the water–binder ratio. However, the limited availability of free water amplified the early hydration characteristics of CSA cement at a water–binder ratio of 0.28, resulting in a synergistic effect. Consequently, small partial replacements of CSA cement had a more pronounced influence at this lower ratio. The CSA cement replacement ratio became the dominant factor affecting the setting process as the mixture stiffened. The results of the green strength and extrusion pressure tests were consistent with the trends observed in the basic material property tests. However, the extrusion pressure test highlighted that increasing the CSA cement replacement ratio also increased viscosity, requiring higher extrusion pressures. Therefore, the appropriate selection of the CSA cement replacement ratio must consider the water–binder ratio, allowable pump pressure, and required open time.
2. Decreasing the water–binder ratio by 0.02 and increasing the CSA cement replacement ratio by 2% resulted in an average reduction of 26.3% and 17.0% in the layer strain, respectively. The effect of the CSA cement replacement ratio was most pronounced at a water–binder ratio of 0.28, consistent with the fresh-state analysis. However, excessively increasing the CSA cement replacement ratio to minimize layer strain may impair extrudability. Therefore, an acceptable tolerance range for layer strain should be defined based on the targeted printing geometry to ensure sufficient open time during printing.
3. The flexural strength of the cast prisms increased as the water–binder ratio decreased, with greater strength gains observed over time at lower ratios. Conversely, the flexural strength decreased as the CSA cement replacement ratio increased, although the rate of strength gain over time remained largely unaffected. For printed prisms, the influence of the water–binder ratio was less pronounced, while the effect of the CSA cement replacement ratio became more evident, indicating its contribution to interlayer bonding performance. Accordingly, interlayer bonding performance tended to improve with higher water–binder ratios and lower CSA cement replacement ratios, and this trend became more prominent with longer curing time.
4. ANOVA and Pareto analysis identified statistically significant factors for both layer strain and interlayer bonding performance, which were used to develop regression models. The adjusted R^2 and predicted R^2 values for the layer strain model were 0.8805 and 0.7228, respectively, while those of the interlayer bonding performance model were 0.6985 and 0.5540. Both models demonstrated sufficient explanatory and predictive capabilities. Response surface analysis showed that neither response exhibited a stationary point, with both response values increasing as the water–binder ratio increased and the CSA cement replacement ratio decreased.
5. Multi-response optimization using the desirability function identified the optimal water–binder and CSA cement replacement ratios of 0.297 and 3.88%, respectively. Verification experiments produced measured values of 0.08638 and 62.2741% for layer strain and interlayer bonding performance, respectively, yielding a mean relative error of 7.55%. These results confirm that the statistical optimization procedure effectively identified an optimized mixture with relatively few experimental trials.

Acknowledgements
Not applicable.

Author Contributions
Sangwoo Oh: conceptualization, methodology, software, formal analysis, investigation, data curation, writing—original draft, writing—review and editing, and visualization. Jinsuk Lee: investigation and data curation. Seongcheol Choi: validation, resources, writing—original draft, writing—review and editing, supervision, project administration, and funding acquisition.

Funding
This work was supported by the National Research Foundation of Korea (NRF) grant funded by the Korea government (MSIT) (RS-2024–00353594); and with the support of the "National R&D Project for Smart Construction Technology (RS-2020-KA156007)" funded by the Korea Agency for Infrastructure Technology Advancement under the Ministry of Land, Infrastructure and Transport, and managed by the Korea Expressway Corporation.

Data Availability
The data sets used and/or analyzed during the current study are available from the corresponding author upon reasonable request.

Declarations

Ethics Approval and Consent to Participate
Not applicable.

Consent for Publication
All authors have reviewed the manuscript and agreed to its submission for publication.

Competing Interest
The authors declare that they have no known competing financial interest or personal relationships that could have influenced the work reported in this paper.

Received: 6 August 2025 Accepted: 3 January 2026
Published online: 12 February 2026

References
ASTM International, Standard Test Method for Flow of Hydraulic Cement Mortar, ASTM C1437–20, 2020. https://doi.org/10.1520/C1437-20.

ASTM International, Standard Practice for Mechanical Mixing of Hydraulic Cement Pastes and Mortars of Plastic Consistency, ASTM C305–20, 2020. https://doi.org/10.1520/C0305-20

ASTM International, Standard Test Method for Flexural Strength of Concrete (Using Simple Beam with Third-Point Loading), ASTM C78/C78M-22, 2022. https://doi.org/10.1520/C0078_C0078M-22.

ASTM International, Standard Test Method for Time of Setting of Concrete Mixtures by Penetration Resistance, ASTM C403/C403M-23, 2023. https://doi.org/10.1520/C0403_C0403M-23.

ASTM International, Standard Test Method for Unconfined Compressive Strength of Cohesive Soil, ASTM D2166/D2166M-24, 2024. https://doi.org/10.1520/D2166_D2166M-24.

Babafemi, A. J., Kolawole, J. T., Miah, M. J., Paul, S. C., & Panda, B. (2021). A concise review on interlayer bond strength in 3D concrete printing. *Sustainability, 13*(13), Article 7137. https://doi.org/10.3390/su13137137

Bescher, E., Rice, E. K., Ramseyer, C., & Roswurm, S. (2016). Sulfate resistance of calcium sulphoaluminate cement. *Journal of Structural Integrity and Maintenance, 1*(3), 131–139. https://doi.org/10.1080/24705314.2016.1211235

Bhattacherjee, S., Basavaraj, A. S., Rahul, A., Santhanam, M., Gettu, R., Panda, B., Schlangen, E., Chen, Y., Copuroglu, O., & Ma, G. (2021). Sustainable materials for 3D concrete printing. *Cement and Concrete Composites, 122*, Article 104156. https://doi.org/10.1016/j.cemconcomp.2021.104156

Bhattacherjee, S., Jain, S., & Santhanam, M. (2024). Investigating the interaction of limestone calcined clay and OPC-based systems with a methyl hydroxyethyl cellulose-based viscosity modifier used for 3D printable concrete. *Journal of Materials in Civil Engineering, 36*(10), Article 04024333. https://doi.org/10.1061/JMCEE7.MTENG-17728

Burris, L. E., & Kurtis, K. E. (2022). Water-to-cement ratio of calcium sulfoaluminate belite cements: Hydration, setting time, and strength development. *Cement, 8*, Article 100032. https://doi.org/10.1016/j.cement.2022.100032

Buswell, R. A., De Silva, W. L., Jones, S. Z., & Dirrenberger, J. (2018). 3D printing using concrete extrusion: A roadmap for research. *Cement and Concrete Research, 112*, 37–49. https://doi.org/10.1016/j.cemconres.2018.05.006

De Schutter, G., Lesage, K., Mechtcherine, V., Nerella, V. N., Habert, G., & Agusti-Juan, I. (2018). Vision of 3D printing with concrete—technical, economic and environmental potentials. *Cement and Concrete Research, 112*, 25–36. https://doi.org/10.1016/j.cemconres.2018.06.001

Ducoulombier, N., Mesnil, R., Carneau, P., Demont, L., Bessaies-Bey, H., Caron, J.-F., & Roussel, N. (2021). The "Slugs-test" for extrusion-based additive manufacturing: Protocol, analysis and practical limits. *Cement and Concrete Composites, 121*, Article 104074. https://doi.org/10.1016/j.cemconcomp.2021.104074

Gołaszewska, M., Gołaszewski, J., & Chmiela, B. (2024). Effect of water to cement ratio on properties of calcium sulfoaluminate cement mortars. *Materials, 17*(12), Article 2806. https://doi.org/10.3390/ma17122806

Hou, D., Chen, D., Wang, X., Wu, D., Ma, H., Hu, X., Zhang, Y., Wang, P., & Yu, R. (2020). RSM-based modelling and optimization of magnesium phosphate cement-based rapid-repair materials. *Construction and Building Materials, 263*, Article 120190. https://doi.org/10.1016/j.conbuildmat.2020.120190

Huang, T., Li, B., Yuan, Q., Shi, Z., Xie, Y., & Shi, C. (2019). Rheological behavior of Portland clinker-calcium sulphoaluminate clinker-anhydrite ternary blend. *Cement and Concrete Composites, 104*, Article 103403. https://doi.org/10.1016/j.cemconcomp.2019.103403

Hung, C.-C., Atmajayanti, A. T., Meiji, V. C. D., Mo, K. H., & Yoo, D.-Y. (2024). Performance of high-strength green strain-hardening cementitious composites incorporating CSA/CAC cements and GGBS. *Structures, 67*, Article 107025. https://doi.org/10.1016/j.istruc.2024.107025

Jiang, Z., Yang, Q., Zhu, Y., Zhang, Y., & Ren, Q. (2022). Evaluating the stiffening effect of CSA and sodium carbonate on the printability of OPC mortar. *Construction and Building Materials, 328*, Article 127088. https://doi.org/10.1016/j.conbuildmat.2022.127088

Ke, G., Zhang, J., & Liu, Y. (2022). Shrinkage characteristics of calcium sulphoaluminate cement concrete. *Construction and Building Materials, 337*, Article 127627. https://doi.org/10.1016/j.conbuildmat.2022.127627

Ke, G., Zhang, J., Xie, S., & Pei, T. (2020). Rheological behavior of calcium sulfoaluminate cement paste with supplementary cementitious materials. *Construction and Building Materials, 243*, Article 118234. https://doi.org/10.1016/j.conbuildmat.2020.118234

Khalil, N., Aouad, G., El Cheikh, K., & Rémond, S. (2017). Use of calcium sulfoaluminate cements for setting control of 3D-printing mortars. *Construction and Building Materials, 157*, 382–391. https://doi.org/10.1016/j.conbuildmat.2017.09.109

Kim, T.-K., Oh, S., Lee, J., Dong, W.-J., Mak, B., Choi, S., & Shim, C.-S. (2025). Effects of 3D-printed concrete permanent formwork on the flexural behavior of reinforced concrete beams: Experimental and analytical investigations. *Case Studies in Construction Materials, 22*, Article e04802. https://doi.org/10.1016/j.cscm.2025.e04802

Kolawole, J. T., De-Becker, D., Xu, J., Dobrzanski, J., Cavalaro, S., Austin, S., Roussel, N., & Buswell, R. (2022). Selected Test Methods for Assessing Fresh and Plastic-State 3D Concrete Printing Materials. In R. Buswell, A. Blanco, S. Cavalaro, & P. Kinnell (Eds.), *Third RILEM International Conference on Concrete and Digital Fabrication* (pp. 460–466). Springer.

Li, M., Weng, Y., Liu, Z., Zhang, D., & Wong, T. N. (2022). Optimizing of chemical admixtures for 3D printable cementitious materials by central composite design. *Materials Science and Additive Manufacturing, 1*, Article 16. https://doi.org/10.18063/msamv1i3.16

Liu, Z., Li, M., Weng, Y., Wong, T. N., & Tan, M. J. (2019). Mixture design approach to optimize the rheological properties of the material used in 3D cementitious material printing. *Construction and Building Materials, 198*, 245–255. https://doi.org/10.1016/j.conbuildmat.2018.11.252

Marchon, D., Kawashima, S., Bessaies-Bey, H., Mantellato, S., & Ng, S. (2018). Hydration and rheology control of concrete for digital fabrication: Potential admixtures and cement chemistry. *Cement and Concrete Research, 112*, 96–110. https://doi.org/10.1016/j.cemconres.2018.05.014

Mechtcherine, V., Bos, F. P., Perrot, A., Da Silva, W. L., Nerella, V., Fataei, S., Wolfs, R. J., Sonebi, M., & Roussel, N. (2020). Extrusion-based additive manufacturing with cement-based materials–Production steps, processes, and their underlying physics: A review. *Cement and Concrete Research, 132*, Article 106037. https://doi.org/10.1016/j.cemconres.2020.106037

Moelich, G. M., Kruger, J., & Combrinck, R. (2021). Modelling the interlayer bond strength of 3D printed concrete with surface moisture. *Cement and Concrete Research, 150*, Article 106559. https://doi.org/10.1016/j.cemconres.2021.106559

Mohan, M. K., Rahul, A., De Schutter, G., & Van Tittelboom, K. (2021). Early age hydration, rheology and pumping characteristics of CSA cement-based 3D printable concrete. *Construction and Building Materials, 275*, Article 122136. https://doi.org/10.1016/j.conbuildmat.2020.122136

Montgomery, D. C. (2020). *Design and analysis of experiments* (10th ed.). Wiley.

Montgomery, D. C., & Runger, G. C. (2020). *Applied statistics and probability for engineers* (7th ed.). Wiley.

Mora, G. S., & Moreno, R. (2021). Rheology and statistical optimization of a shear-sensitive fluid as a treatment for circulation loss control. *Journal of Petroleum Science and Engineering, 205*, Article 108830. https://doi.org/10.1016/j.petrol.2021.108830

Muthukrishnan, S., Ramakrishnan, S., & Sanjayan, J. (2021). Technologies for improving buildability in 3D concrete printing. *Cement and Concrete*

Composites, 122, Article 104144. https://doi.org/10.1016/j.cemconcomp.2021.104144
Myers, R. H., Montgomery, D. C., & Anderson-Cook, C. M. (2016). *Response surface methodology: Process and product optimization using designed experiments* (4th ed.). Wiley.
Oh, S., & Choi, S. (2023). Effects of superabsorbent polymers (SAP) on the rheological behavior of cement mortars: A rheological study on performance requirements for 3D printable cementitious materials. *Construction and Building Materials, 392*, Article 131856. https://doi.org/10.1016/j.conbuildmat.2023.131856
Oh, S., Hong, G., & Choi, S. (2021). Literature review on rheological properties and required performances of 3D printable cementitious materials. *Journal of the Korean Recycling Construction Resources Institute, 9*(1), 41–49. https://doi.org/10.14190/JRCR.2021.9.1.41
Oh, S., Hong, G., & Choi, S. (2023). Determining the effect of superabsorbent polymers, macrofibers, and resting time on the rheological properties of cement mortar using analysis of variance (ANOVA): A 3D printing perspective. *Journal of Building Engineering, 75*, Article 106967. https://doi.org/10.1016/j.jobe.2023.106967
Park, S., Jeong, Y., Moon, J., & Lee, N. (2021). Hydration characteristics of calcium sulfoaluminate (CSA) cement/portland cement blended pastes. *Journal of Building Engineering, 34*, Article 101880. https://doi.org/10.1016/j.jobe.2020.101880
Paul, S. C., Van Zijl, G. P., Tan, M. J., & Gibson, I. (2018). A review of 3D concrete printing systems and materials properties: Current status and future research prospects. *Rapid Prototyping Journal, 24*(4), 784–798. https://doi.org/10.1108/RPJ-09-2016-0154
Pelletier-Chaignat, L., Winnefeld, F., Lothenbach, B., Le Saout, G., Müller, C. J., & Famy, C. (2011). Influence of the calcium sulphate source on the hydration mechanism of Portland cement–calcium sulphoaluminate clinker–calcium sulphate binders. *Cement and Concrete Composites, 33*(5), 551–561. https://doi.org/10.1016/j.cemconcomp.2011.03.005
Reiter, L., Wangler, T., Anton, A., & Flatt, R. J. (2020). Setting on demand for digital concrete–principles, measurements, chemistry, validation. *Cement and Concrete Research, 132*, Article 106047. https://doi.org/10.1016/j.cemconres.2020.106047
Reiter, L., Wangler, T., Roussel, N., & Flatt, R. J. (2018). The role of early age structural build-up in digital fabrication with concrete. *Cement and Concrete Research, 112*, 86–95. https://doi.org/10.1016/j.cemconres.2018.05.011
Roussel, N. (2018). Rheological requirements for printable concretes. *Cement and Concrete Research, 112*, 76–85. https://doi.org/10.1016/j.cemconres.2018.04.005
Sergis, V., & Ouellet-Plamondon, C. M. (2022). Automating mix design for 3D concrete printing using optimization methods. *Digital Discovery, 1*(5), 645–657. https://doi.org/10.1039/D2DD00040G
Sirtoli, D., Wyrzykowski, M., Riva, P., & Lura, P. (2020). Autogenous and drying shrinkage of mortars based on Portland and calcium sulfoaluminate cements. *Materials and Structures, 53*, Article 126. https://doi.org/10.1617/s11527-020-01561-1
Strohle, M., Sadique, M., Dulaimi, A., & Kadhim, M. A. (2023). Prospect and barrier of 3D concrete: A systematic review. *Innovative Infrastructure Solutions, 8*(1), Article 21. https://doi.org/10.1007/s41062-022-00975-w
Subasi, A., Sahin, B., & Kaymaz, I. (2016). Multi-objective optimization of a honeycomb heat sink using Response Surface Method. *International Journal of Heat and Mass Transfer, 101*, 295–302. https://doi.org/10.1016/j.ijheatmasstransfer.2016.05.012
Tabachnick BG, Experimental designs using ANOVA, Thomson/Brooks/Cole, Belmont, CA, 2007.
Tran, M. V., Le, T. T., Cao, N. T., & Nguyen, T. H. Y. (2025). Sustainable prospect for entire replacement of river sand with recycled glass aggregate in 3D printing concrete: Rheological properties, printability, and alkali-silica reaction. *Journal of Materials in Civil Engineering, 37*(6), Article 04025164. https://doi.org/10.1061/JMCEE7.MTENG-18746
Tran, N., Tran, M. V., Tran, P., Nguyen, A. K., & Nguyen, C. Q. (2024). Eco-friendly 3D-printed concrete using steel slag aggregate: Buildability, printability, and mechanical properties. *International Journal of Concrete Structures and Materials, 18*, Article 66. https://doi.org/10.1186/s40069-024-00705-9
Trauchessec, R., Mechling, J.-M., Lecomte, A., Roux, A., & Le Rolland, B. (2015). Hydration of ordinary Portland cement and calcium sulfoaluminate cement blends. *Cement and Concrete Composites, 56*, 106–114. https://doi.org/10.1016/j.cemconcomp.2014.11.005
Wang, L., Tian, Z., Ma, G., & Zhang, M. (2020). Interlayer bonding improvement of 3D printed concrete with polymer modified mortar: Experiments and molecular dynamics studies. *Cement and Concrete Composites, 110*, Article 103571. https://doi.org/10.1016/j.cemconcomp.2020.103571
Wang, S., Li, B., Zeng, H., Liang, C., & Zhang, G. (2024). Comparison of mechanical strengths and microstructure of Portland cement-calcium sulfoaluminate cement binders with cellulose ethers of different viscosities. *Construction and Building Materials, 437*, Article 137022. https://doi.org/10.1016/j.conbuildmat.2024.137022
Wang, S., Wang, Z., Huang, T., Wang, P., & Zhang, G. (2022a). Mechanical strengths, drying shrinkage and pore structure of cement mortars with hydroxyethyl methyl cellulose. *Construction and Building Materials, 314*, Article 125683. https://doi.org/10.1016/j.conbuildmat.2021.125683
Wang, S., Zhang, G., Wang, Z., Huang, T., & Wang, P. (2022b). Evolutions in the properties and microstructure of cement mortars containing hydroxyethyl methyl cellulose after controlling the air content. *Cement and Concrete Composites, 129*, Article 104487. https://doi.org/10.1016/j.cemconcomp.2022.104487
Wolf, J., Jansen, D., Goetz-Neunhoeffer, F., & Neubauer, J. (2021). Relating phase transitions to pore size distributions and mechanical mortar properties in CSA-OPC-C $ based systems–The potential impact of delayed straetlingite formation. *Cement and Concrete Research, 147*, Article 106496. https://doi.org/10.1016/j.cemconres.2021.106496
Wolfs, R., Versteege, J., Santhanam, M., Bhattacherjee, S., Bos, F., Robens-Radermacher, A., Muthukrishnan, S., Menna, C., Ozturk, O., Ozyurt, N., Roupec, J., Richter, C., Jungwirth, J., Miranda, L., Ammann, R., Caron, J.-F., de Bono, V., Monte, R., Navarrete, I., … Mechtcherine, V. (2025). Mechanical properties of 3D printed concrete: A RILEM TC 304-ADC interlaboratory study – flexural and tensile strength. *Materials and Structures, 58*(5), Article 182. https://doi.org/10.1617/s11527-025-02687-w
Xie, C., Cao, M., & Lv, X. (2021). Optimization of calcium carbonate whisker reinforced cement paste for rheology and fracture properties using response surface methodology. *Fatigue & Fracture of Engineering Materials & Structures, 44*(3), 859–875. https://doi.org/10.1111/ffe.13403
Xie, Z., Yao, H., Yuan, Q., & Zhong, F. (2023). The roles of water-soluble polymers in cement-based materials: A systematic review. *Journal of Building Engineering, 73*, Article 106811. https://doi.org/10.1016/j.jobe.2023.106811
Yang, Z., Ye, H., Yuan, Q., Li, B., Li, Y., & Zhou, D. (2021). Factors influencing the hydration, dimensional stability, and strength development of the OPC-CSA-anhydrite ternary system. *Materials, 14*(22), Article 7001. https://doi.org/10.3390/ma14227001
Yin, Y., Huang, J., Wang, T., Yang, R., Hu, H., Manuka, M., Zhou, F., Min, J., Wan, H., Yuan, D., & Ma, B. (2023). Effect of hydroxypropyl methyl cellulose (HPMC) on rheology and printability of the first printed layer of cement activated slag-based 3D printing concrete. *Construction and Building Materials, 405*, Article 133347. https://doi.org/10.1016/j.conbuildmat.2023.133347
Yu, S., Xia, M., Sanjayan, J., Yang, L., Xiao, J., & Du, H. (2021). Microstructural characterization of 3D printed concrete. *Journal of Building Engineering, 44*, Article 102948. https://doi.org/10.1016/j.jobe.2021.102948
Zhang, C., Nerella, V. N., Krishna, A., Wang, S., Zhang, Y., Mechtcherine, V., & Banthia, N. (2021). Mix design concepts for 3D printable concrete: A review. *Cement and Concrete Composites, 122*, Article 104155. https://doi.org/10.1016/j.cemconcomp.2021.104155
Zhang, J., Li, G., Ye, W., Chang, Y., Liu, Q., & Song, Z. (2018). Effects of ordinary Portland cement on the early properties and hydration of calcium sulfoaluminate cement. *Construction and Building Materials, 186*, 1144–1153. https://doi.org/10.1016/j.conbuildmat.2018.08.008
Zhang, Y., Qiao, H., Qian, R., Xue, C., Feng, Q., Su, L., Zhang, Y., Liu, G., & Du, H. (2022). Relationship between water transport behaviour and interlayer voids of 3D printed concrete. *Construction and Building Materials, 326*, Article 126731. https://doi.org/10.1016/j.conbuildmat.2022.126731

Publisher's Note

Springer Nature remains neutral with regard to jurisdictional claims in published maps and institutional affiliations.

Sangwoo Oh PhD student in Chung-Ang University, Department of Civil and Environmental Engineering, 84 Heukseok-ro, Dongjak-gu, Seoul 06974, Republic of Korea

Jinsuk Lee PhD student in Chung-Ang University, Department of Smart Cities, 84 Heukseok-ro, Dongjak-gu, Seoul 06974, Republic of Korea

Seongcheol Choi Professor in Chung-Ang University, Department of Civil and Environmental Engineering, 84 Heukseok-ro, Dongjak-gu, Seoul 06974, Republic of Korea